UNIVERSIDADE ESTADUAL DE CAMPINAS
Instituto de Física Gleb Wataghin

MATHEUS MELO SANTOS VELLOSO

Otimização Online da Abertura Dinâmica do SIRIUS

Online Optimization of SIRIUS Dynamic Aperture

CAMPINAS

2024

MATHEUS MELO SANTOS VELLOSO

Online Optimization of SIRIUS Dynamic Aperture

Otimização Online da Abertura Dinâmica do SIRIUS

Dissertação apresentada ao Instituto de Física Gleb Wataghin da Universidade Estadual de Campinas como parte dos requisitos exigidos para a obtenção do título de MESTRE EM FÍSICA, na Área de FÍSICA.

Thesis presented to the Gleb Wataghin Institute of Physics of the University of Campinas in partial fulfillment of the requirements for the degree of MASTER IN PHYSICS, in the area of PHYSICS.

Orientadora: LIU LIN

Coorientador: ANTONIO RUBENS BRITTO DE CASTRO

ESTE TRABALHO CORRESPONDE À VERSÃO PRELIMINAR DA TESE A SER DEFENDIDA PELO ALUNO MATHEUS MELO SANTOS VELLOSO E ORIENTADA PELA DRA. LIU LIN.

CAMPINAS

2024

FICHA CATALOGRÁFICA

FOLHA DA APROVAÇÃO

Agradecimentos

Primeiramente, agradeço à minha orientadora, Liu. Sua experiência e seu direcionamento foram fundamentais para o sucesso deste projeto. Agradeço por todo apoio, incentivo, paciência e pela oportunidade de participar deste projeto e de trabalhar junto a pessoas tão experientes e inspiradoras num ambiente tão estimulate e rico.

Agradeço também ao Professor Rubens pela coorientação. Obrigado pelo interesse constante no trabalho e por se fazer sempre presente, além de sempre ter feito questão de oferecer belas palavras de congratulação e reconhecimento das pequenas conquistas.

Agradeço aos meus pais e familiares. Obrigado pelo constante apoio, compreensão e paciência, especialmente pelas minhas ausências. Também agradeço à minha companheira, cujo amor, carinho e apoio foram minhas principais fontes de força e conforto. Obrigado, Juba.

Sou grato aos funcionários do CNPEM e do LNLS, pelo esforço conjunto para erquer um ambiente único para a ciência e tecnologia no Brasil. Aos colegas do grupo de Física de Aceleradores (FAC) do LNLS, sou extremamente grato pela colaboração e momentos de descontração compartilhados durante todo o período de trabalho. Obrigado Fernando, Murilo, Ximenes e Gabriel pelas discussões valiosas e sempre muito produtivas, pela leitura desta dissertação, e por toda a colaboração durante este projeto. Aprendi muito com vocês e espero ainda aprender muito mais. Agradeço também ao Gustavo, Thales, Vitor, Raphael, Filipe e Jucelio pelos momentos que compartilhamos em 2022 e 2023.

Sou grato ao IFGW pela infraestrutura proporcionada durante o mestrado e pela oportunidade de ter acesso aos cursos avançados e contato com os excelente professores. Em especial, agradeço ao professor Amir Caldeira por suas excelentes aulas de mecânica quântica e ao professor Marcos Aguiar pelo excelente curso de de mecânica avançada. Agradeço também aos professores Diego Muraca, José Brum e Alexandre Fonseca pela orientação durante minha atuação no programa de estágio docente, e aos funcionários do programa de pós-graduação, em especial à Cristina, pelo atendimento proativo e atencioso.

Também gostaria de expressar minha gratidão aos professores e pesquisadores que contribuíram com críticas e sugestões construtivas para este trabalho. Além de minha orientadora, coorientador e colegas da FAC, agradeço pelo feedback dos professores José Brum, Eduardo Granado e Júlio Criginski, durante o exame de qualificação, e pelo feedback de Túlio Rocha e Eduardo Miqueles, durante no seminário de pré-requisito.

Por fim, expresso minha gratidão às agências de fomento CAPES e FAPESP

Resumo

O acúmulo de feixe no anel de armazenamento do SIRIUS ocorre no esquema de injeção *off-axis*, o qual depende de uma abertura dinâmica (AD) – a região contemplando oscilações transversais estáveis – suficientemente grande. Antes do trabalho de otimização, a AD do SIRIUS se mostrava suficientemente grande para fornecer uma boa eficiência de injeção, mas também mostrava sinais de que poderia ainda ser melhorada por meio do ajuste fino das forças dos imãs sextupolos, que determinam a AD. Neste projeto de mestrado, o alogritmo *Robust Conjugate Direction Search* (RCDS) para otimização online foi aplicado para otimizar a AD e eficiência de injeção no SIRIUS. Os experimentos também foram realizados em outros pontos de operação, com maiores valores para a parte fracionária das sintonias. Aumentar as sintonias é benéfico para a estabilidade órbita, mas geralmente deteriora a AD, o que requer o trabalho de otimização online para alcançar valores de eficiência de injeção que atendam as demandas da operação. Este trabalho mostra como a otimização online foi bem sucedida para otimizar a AD no ponto de operação nominal do SIRIUS, bem como em um novo ponto de operação, onde melhorias na estabilidade de órbita foram observadas. Os resultados salientam a efetividade desse método em anéis de armazenamento de 4º geração.

Abstract

Electron beam accumulation into SIRIUS storage ring occurs in a off-axis scheme, on which the efficiency depends on a sufficiently large dynamic aperture (DA): the region comprising stable transverse oscillations. Prior to optimization, SIRIUS DA was sufficiently large for providing good injection efficiency levels, but showed signs it could be further improved upon fine-tuning of sextupole magnet strengths, which determine the DA. In this master's project, the Robust Conjugate Direction Search Algorithm (RCDS) for online optimization was applied to optimize the DA and the injection efficiency at SIRIUS. Online optimization was also carried out in different working points, with higher fractional tunes. Higher tunes are beneficial for orbit stability, but usually deteriorate the DA, requiring online optimization work to achieve injection efficiencies meeting operation demands. This work shows how online optimization was successful at optimizing the DA in SIRIUS nominal working point as well as in a new working point where orbit stability improvements were observed. The results highlight the effectiveness of this method in 4th-generation storage rings.

List of Figures

List of Tables

Glossary

4GSR 4th generation storage ring. 16, 45

5BA five-bend-achromat. 51, 52

ALBA "Sunrise" in Catalan and in Spanish. A third-generation synchrotron light source facility in the Barcelona Synchrotron Park in Cerdanyola del Vallès, near Barcelona. 15

ALS Advanced Light Source. 15

APS Advanced Photon Source. 15

BESSY Berliner Elektronenspeicherring-Gesellschaft für Synchrotronstrahlung. 15

BPM Beam Position Monitor. 52–55, 64, 67, 70, 72, 74

CNPEM Brazilian Center for Research in Energy and Materials. 16

DA Dynamic Aperture. 14, 20–22, 40–45, 57–59, 64–71, 73, 75, 76

DCCT Direct-Current Current Transformer. 54, 67

DESY Deutsches Elektronen-Synchrotron. 15

DORIS Double-Ring Storage Facility. 15

ELETTRA Third-generation electron storage ring of the Elettra Sincrotrone Trieste research center, in Trieste, Italy. 15

ELSA Electron Stretcher Accelerator. 15

ESRF European Synchrotron Radiation Facility. 15, 16, 45

ID insertion device. 15

IE Injection Efficiency. 14, 21, 22, 54, 57, 63–66, 68–73, 75–77

KEK Japanese High Energy Accelerator Research Organization. 15

LINAC Linear Accelerator. 16, 17

LNLS Brazilian Synchrotron Light Laboratory. 16, 17, 50

Contents

Introduction

This dissertation focuses on the work conducted on the SIRIUS storage ring with the objective of optimizing the ring's Dynamic Aperture (DA) and Injection Efficiency (IE). The text is structured as follows:

- The current chapter introduces synchrotron light sources, provides an overview of the SIRIUS project, outlines the main components and subsystems present in electron storage rings, and elucidates the problem addressed in this work;

- Chapter 1 delves into the theoretical and scientific background regarding the dynamics of particles in accelerators. It covers topics such as optics functions, tunes, chromatic effects, field errors, perturbations, and the dynamic aperture;

- Chapter 2 introduces the online optimization of nonlinear dynamics in accelerators and presents the Robust Conjugate Direction Search (RCDS) algorithm;

- Chapter 3 presents the diagnostic tools available for probing the electron beam's motion, current, and other relevant parameters. It also covers technical details on the design of the experiments and measurements reported here, such as the choice of the objective function and the decision variables for the optimization problem;

- Chapter 4 presents the results of the online optimization experiments and discusses their significance for the machine operation and stability.

- Lastly, Chapter 5 provides conclusions and closing remarks on the findings and implications of the study.

Storage ring-based synchrotron light sources

Synchrotron radiation (SR) is the electromagnetic radiation emitted by charged relativistic particles when accelerated perpendicularly to their motion. The phenomenon was theoretically predicted in the early 1900s when Liénard and Wiechert calculated the retarded potentials for point particles. The first experimental observation in a laboratory occurred at General Electric's synchrotron accelerator, justifying the adoption of the term "synchrotron" in its name [1].

Synchrotron light is extremely collimated and has a broad spectral distribution, covering from infrared to hard X-rays. These properties make it ideal for imaging experiments in crystallography and spectroscopy across a wide variety of scientific disciplines.

Modern synchrotron light sources rely primarily on two particle acceleration technologies: free-electron lasers and electron storage rings. Here we focus on storage

ring-based synchrotron light source facilities. In these facilities, ultra-relativistic electron beams are stored for extended periods around a closed orbit within a chamber in ultra-high vacuum to produce synchrotron light. The beam is maintained in stable orbits by the fields of magnets carefully placed along the ring to provide bending and focusing of the electrons trajectories. It is also periodically influenced by longitudinal standing-wave electric fields in the radio-frequency range, which replenish the energy radiated away in the form of light.

The main figure of merit for measuring the quality of a SR source is the *brightness* [2], defined as the photon flux density in phase space [1,3]:

$$B(\omega) = \frac{1}{\Delta\omega/\omega} \frac{\dot{N}(\omega)}{4\pi^2 \Sigma_x(\omega)\Sigma_y(\omega)}, \tag{1}$$

where $\dot{N}$ is the photon flux at energies in $E = \hbar\omega$, $E + \mathrm{d}E$. Σ_u is the photon beam volume in the $u = x, y$ phase space, and $\Delta\omega/\omega$ is the frequency bandwidth. The photon phase space volume depends on the convolution of the electron beam distribution with the distribution of the photons emitted by a single electron. The latter depends on the photon energy and the emission process, while the former is related to the phase space volume of the electron beam: the *emittance.* The equilibrium beam emittance depends on the magnetic lattice and has units of the transverse phase space areas (size × angle). Increasing brightness can be achieved by maximizing the photon flux, reducing the electron beam emittances and optimizing the matching between photon and electron beams distribution orientation. [1].

Synchrotron light sources can be classified based on their brightness and emittance. In the early 1960s, the community interested in SR for imaging experiments obtained it parasitically from machines originally designed for high-energy and nuclear physics experiments, such as DESY and DORIS, in Germany, and ADA, in Italy [4]. This marks the era of the first-generation synchrotron light sources [5]. The second-generation machines emerged in the 1980s and consisted on machines designed exclusively for SR production, such as BESSY, DORIS II, DORIS III, and ELSA, in Germany; SuperACO, in France; MAX I, in Sweden [4]; NSLS and SPEAR, in the USA; UVX in Brazil; KEK Photon Factory and SOR-Ring, in Japan.

The 1990s saw a growing demand for higher brightness, leading to the development of third-generation machines [5]. These machines introduced insertion devices (IDs) such as wigglers and undulators, which consist of a sequence of alternating magnetic fields generally created by an array of permanent magnets arranged in a Halbach array [6, chapter 7]. IDs significantly enhance brightness by adding the radiation emitted by many poles. They also allowed precise control over the emitted radiation energy and polarization.

Typical emittances for third-generation machines is of the order of units to tens of nm.rad. Most of the currently operating machines pertain to the third-generation,

such as ALBA, in Spain; SOLEIL and ESRF, in France; Diamond, in the United Kindom; ELETTRA, in Italy [4]; SPEAR3, APS, ALS and NSLS-II, in the USA; SSRF, in China; Spring-8 in Japan; PLS-II, in Korea; TPS, in Taiwan; CLS, in Canada; and AS, in Australia

The era of the 4th generation storage rings (4GSRs) commenced with the design of the MAX-IV machine in Lund, Sweden, in 2015 [3, 5]. 4GSRs achieved a notable reduction in emittance, reaching sub-nm.rad values thanks to recent technological advancements in accelerator technology, such as computer simulations, vacuum technology, machining, mechanical alignment, and others [3, 5]. Following MAX-IV, an upgrade of the ESRF facility, the ESRF-EBS, in France, and the launch of SIRIUS, in Campinas, Brazil, marked significant milestones for the fourth-generation. Today, several 4GSR projects are being planned, designed and constructed around the globe.

The SIRIUS project

SIRIUS is a 4GSR synchrotron light source. It was designed, built, and is operated by the Brazilian Synchrotron Light Laboratory (LNLS), on the campus of the Brazilian Center for Research in Energy and Materials (CNPEM), in Campinas, Brazil. The electron storage ring has 518 m in circumference and its operating energy is 3 GeV. The natural emittance of the lattice is 250 pm.rad.

SIRIUS succeeded the first synchrotron light source in Brazil, the UVX machine, which opened to users in 1997 and served the community until its shutdown, in the beginning of SIRIUS commissioning, in August 2019 [7]. The SIRIUS project started in 2009, initially planned and designed as a third-generation machine. By 2012, the project evolved into that of a 4GSR [7]. Building construction was finished in 2018, the LINAC and Booster commissioning soon followed. In November 2019 the first beam was stored in the storage ring.

SIRIUS finished the Phase-0 commissioning in 2022 and since March 2023 is receiving the first external users. At the time of this writing, it has 10 operating beamlines, 1 beamline in commissioning, 2 under construction and 1 beamline in design [8]. The storage ring currently stores 100 mA current, operating with frequent beam injections throughout the day, a scheme known as "top-up" mode. SIRIUS is expected to achieve 350 mA current when the system of two superconducting radio-frequency (RF) cavities and the third-harmonic cavity are installed [9, 10].

Presently, SIRIUS stands as the most complex scientific infrastructure ever constructed in Brazil, aiming to position the country at the forefront of global leadership in synchrotron light science and technology. It has the capacity to host up to 40 beamlines and as of the time of this writing, SIRIUS is the sole fourth-generation synchrotron light source in the southern hemisphere and one of merely three 4GSRs in operation across the globe.
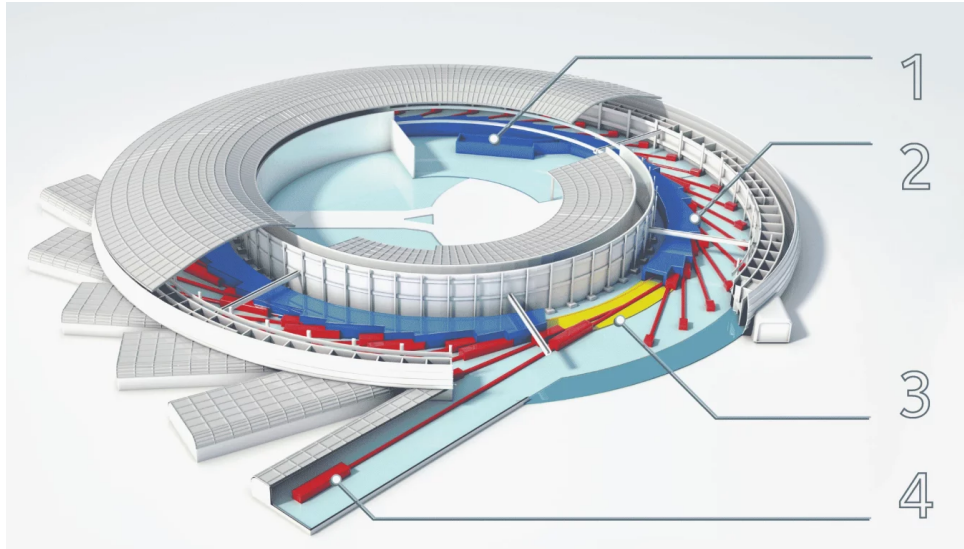
Figure 1: Schematic view of the SIRIUS installations. 1) Linear Accelerator (LINAC); 2) Concrete tunnel housing the booster accelerator and the storage ring, in blue; 3) tunnel interior floor, in yellow; beamlines, in red, long beamlines, in 4). Figure from LNLS website.

Physics of electron storage rings: an overview

Typical systems comprising a storage ring synchrotron light source facility include:

- an injection system: including the electrons source, beam transport lines, the linear accelerator and the booster synchrotron accelerator. At SIRIUS, the linear accelerator provides the booster with a 150 MeV beam. The booster further ramps the beam energy up to 3 GeV, which is the storage ring operation energy;

- storage ring: where the ultra-relativistic beam of electrons is kept in stable orbits for hours within the vacuum-chamber, producing synchrotron light at the bending magnets and insertion devices;

- beamlines which steer, focus and select the energy of the photon beams towards the experimental cabins where samples are placed for the experiments based on light-matter interaction, such as spectroscopy, crystallography, tomography and others.

A schematic view of the SIRIUS building is shown in Fig. 1.

Figure 2 outlines the typical layout of a synchrotron storage ring. The electron beam is stored within a vacuum chamber, where the individual electrons oscillate in proximity to a reference closed orbit, under the influence of magnetostatic fields from an array of multipolar magnets (the magnetic lattice) and also time-dependent fields from the RF cavities.

A pure dipole magnet provides a uniform and homogeneous magnetic field perpendicular to the facility floor and bends the electron's trajectory in the plane parallel
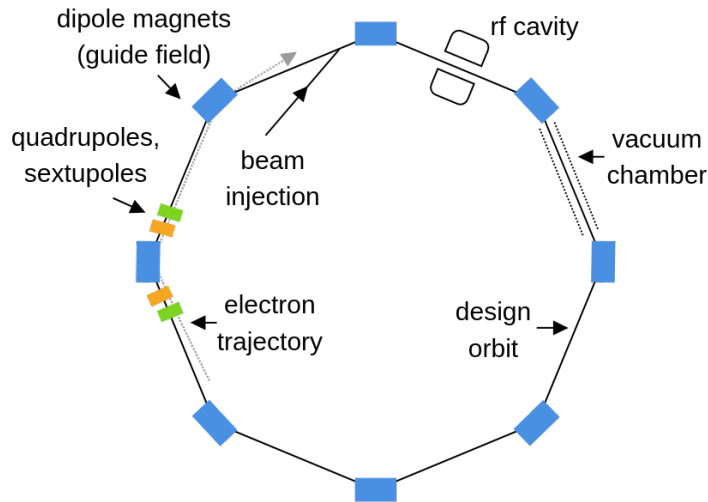
Figure 2: Storage ring typical configuration. Inspired by ref. [11]

to the floor. The field profile of a dipole magnet is depicted in the left-side sketch of Fig. 3. Imagining a beam directed inward toward the screen, the trajectory will be bent to the right. For trajectories resulting in a closed orbit, the overall bending angle provided by the dipoles along the entire ring must equal 2π radians.

To maintain electrons in close proximity to the reference orbit, focusing of the trajectories is required. Focusing is attained by employing gradient fields, primarily generated by quadrupole magnets. The strength of such fields increases linearly with deviations from the closed orbit, which lies in the magnet's center. Gradient fields effectively act as restoring spring forces. The magnets poles and the field profile of a quadrupole magnet are depicted in the center sketch of Fig. 3.

Focusing and deflection are energy-dependent, which means small deviations from the nominal operating energy can result in an enlarged or reduced orbit and on differential focusing at the gradients. The former effect is a dispersion effect, while in the latter, drawing an analogy from geometric optics, the beam's focusing behavior at the "lenses" (quadrupoles) depends on its "color" (energy). The sextupole fields serve as corrective lenses to correct these chromatic aberrations. They introduce geometric aberrations to counteract the chromatic ones, resulting in approximately uniform, energy-independent focusing, up to the linear approximation. The magnets poles and the field profile of a sextupole magnet are depicted in the right sketch of Fig. 3.

Besides dipoles, quadrupoles and sextupoles, additional dipole actuators magnets for orbit/trajectory correction and pulsed magnets for beam injection can also be found in the ring.

When having its trajectory bent at the dipoles and insertion devices, the beam loses energy in the form of synchrotron radiation. To avoid inward spiraling and to maintain the beam stored, the energy lost must be replenished. To achieve this, RF cavities are placed along the ring to provide oscillating electric fields along the longitudinal
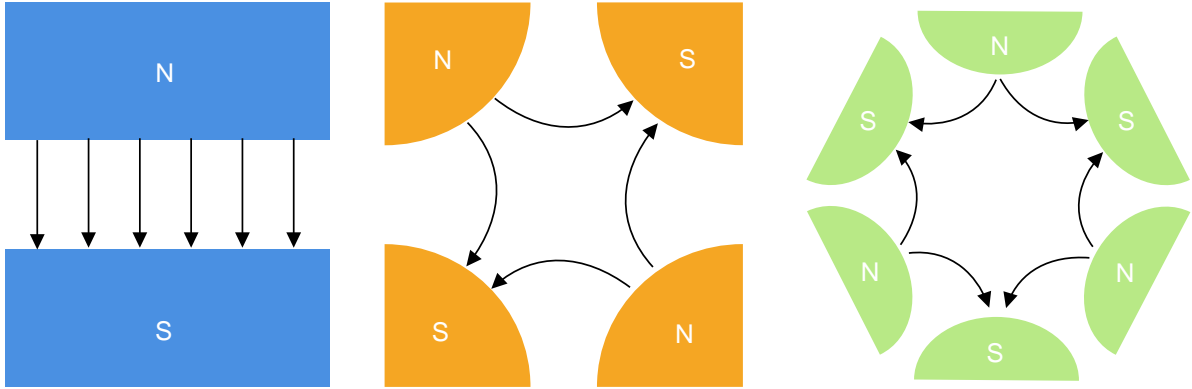
Figure 3: Schematic representation of the magnets comprising SIRIUS lattice and their fields profile. From left to right: dipole magnet, quadrupole magnet and sextupole magnet.

direction. The work done in the beam by the fields restore its energy.

The radiated photons are instantaneously emitted in a narrow cone with angular aperture of $1/\gamma$, γ being the relativistic Lorentz factor (~ 6000 at SIRIUS storage ring). The photons carry away a fraction of the beam's momentum in both the longitudinal and transverse directions. However, when passing through RF cavities, only momentum in the longitudinal direction is replenished. The combined effect of radiating photons and passing through RF cavities leads to an overall damping of the transverse oscillations amplitudes.

On the other hand, the quantum nature of the emitted radiation leads to the excitation of transverse oscillations, an effect known as quantum excitation. When a photon carries away energy, it depletes the electrons energy by the same amount. It thus changes the reference orbit of the electron because of the dispersion effect, inducing oscillations. Additionally, coupling on the transverse plane and intra-beam scattering events can lead to the excitation of transverse oscillations, enlarging the beam size. Eventually, equilibrium between radiative damping and transverse excitations is achieved, leading the beam size to reach a stationary value.

Each degree of freedom of the beam (transverse amplitudes and momenta, beam energy and revolution time) defines an acceptance, which establishes limits on the dynamical variables. Exceeding these limits can result in unstable, unbounded motion, and eventually, beam losses. The most apparent form of acceptance is the transverse acceptance, since the beam motion is bounded by a vacuum chamber, and colliding with the chamber's physical aperture leads to losses. Additionally, the beam has an energy acceptance, representing a tolerance for energy deviations from the nominal value. Exceeding this tolerance can lead to a unstable energetic balance when passing at the RF cavities. Over the span of several turns, the energy deviations can grow and result in significant deviations from the nominal orbit because of the dispersive effect. Eventually

the beam collides with the vacuum chamber wall.

Because of the nonlinearities introduced mainly by the sextupole magnets, the transverse acceptances can be limited not solely by the physical aperture available in the vacuum chamber but rather by the amplitudes above which motion is irregular, unstable and unbounded. This limiting amplitude is known as the Dynamic Aperture DA, a term that can be used to refer to the limiting amplitudes in the transverse space x, y as well as the phase space coordinates x, p_x and y, p_y.

Knowledge of the acceptances and the distribution for the values of the dynamical variables, which can be well approximated by a Gaussian distribution, allows the determination of the expected rate at which the variables exceed the acceptances, defining the base rate for the expected beam loss in the ring. Additionally, the beam is also susceptible to elastic and inelastic collisions with residual gas molecules within the chamber, as well as collisions between electrons within the same bunch. All these effects can lead to beam loss, and the overall beam loss rate resulting from these combined mechanisms defines the characteristic time scale during which a given electron current survives in the ring. This is the beam lifetime and determines the rate at which injections into the storage ring are required to maintain the current within a specified range.

The problem addressed in this work

The pursuit of low-emittances and high-brightness has propelled the accelerator community toward the fourth-generation of storage rings. Achieving such low emittances was made possible by a series of technological advances that enabled the use of the Multi-Bend-Achromat (MBA) lattice [3,5]. MBA lattices require intense gradient fields provided by quadrupole magnets, which, in turn, demand the presence of strong sextupolar fields to compensate for chromatic effects. As sextupoles introduce nonlinear fields, the dynamics in fourth-generation storage rings has become increasingly nonlinear [5].

A quasi-periodic nonlinear dynamics when subjected to perturbations, such as small field errors stemming from rotation, alignment, or fields excitation errors, can potentially become unstable at large oscillation amplitudes. These instabilities impose constraints on the maximum transverse oscillation amplitudes that the machine can accommodate, the DA of the ring. Exceeding the DA results in irregular and often chaotic motion and beam loss.

Under normal operation conditions, the equilibrium beam size and the typical oscillation amplitudes are considerably smaller than the DA , and the dynamics can be well studied and analyzed using a linear approximation theory, without worrying about the DA. However, there are specific scenarios where the DA becomes crucial for the operation, notably during the injection process.

During injection into the storage ring for beam accumulation, the beam is

extracted from the booster accelerator and guided toward the storage ring through a transport line. Upon entering the ring, the beam is deflected by the field of a pulsed nonlinear magnet, aligning the beam almost parallel to the storage ring tangent direction, albeit with a horizontal offset of approximately $x = -8$ mm [12]. If the DA is smaller than this initial amplitude at the injection point, it imposes limitations on the IE.

The DA is determined by the beam's nonlinear dynamics performance, which is a consequence of the nonlinear lattice (sextupoles). In the design phase of the SIRIUS project, the placement, symmetry, and strength of sextupole magnets were determined through a multi-objective optimization process, primarily focused on improving the simulated DA and beam lifetime of the machine's computer model [13,14]. This optimization work considered the average performance of the lattice configurations while accounting for various magnet errors that simulate the expected errors in the actual machine [13]. Several models (lattice configurations), with errors distributed among the magnets, were generated, and the DA and lifetime for a given lattice configuration were calculated by simulating the electron beam's motion for thousands of turns (tracking simulations). The final figure of merit for a magnetic lattice consisted of the average DA and lifetime it provided to the ensemble of machines. The best-performing machine lattice found during this process was adopted as the nominal lattice and subsequently deployed during the commissioning phase of the machine. Prior to the optimization work reported here, the machine operated with this nominal sextupole configuration.

The real machine consists of a practical realization of one specific error configuration, which defines the physically realized magnetic lattice and determines the overall performance of the dynamics. The nominal nonlinear lattice, identified as the best-performing lattice on average in simulations, is not necessarily the optimum lattice for this specific error realization.

Assuming the realized lattice closely approximates the optimum setup, i.e., that the errors are small, it is reasonable to assume that by making minor tweaks and adjustments to the sextupoles, one can adapt the nonlinear lattice to the actual distribution of errors in the physical system. Since the sextupoles are already installed, the optimization variables available are their field strengths. A fine-tuning of strengths aiming to accommodate the nonlinear fields to the realized lattice can result in improvements to the nonlinear dynamics performance, increases in the DA, and an enhancement of IE.

This sextupole tuning process has already been demonstrated in other machines [15–19]. It has proven to be a successful approach and consists of a particular application of *Online optimization*. If one thinks of the errors as agents responsible for deteriorating the DA from its optimum, online optimization of nonlinear dynamics can be seen as an attempt to compensate for such deterioration.

Online optimization of the machine nonlinear dynamics consists of employing computer-automated search strategies to systematically explore various sextupole

configurations with the goal of identifying the ones that yield the largest DA while not interfering with other machine parameters, such as chromaticity and beam lifetime. The key ingredient in online optimization is the choice of a robust optimization algorithm based on direct or indirect search in the parameter space. The most widely used is the RCDS algorithm [15], which is based on a noise-robust one-dimensional optimizer along with a clever strategy, known as Powell's method, for choosing directions in the search space. Chapter 2 addresses the RCDS algorithm.

Besides improving the DA and IE in nominal operation conditions, it is also interesting, and in some cases it is necessary, to do so in different machine *working points*, with different *tunes*. As presented in chapter 1, if one fixes one's attention to a specific point of the ring, and measure the beam position in horizontal and vertical planes for consecutive turns, one realizes the motion is a sampled sinusoid and the fractional parts of the tunes ν_x and ν_y are the fundamental frequencies of such harmonic motion on each plane. The tunes are important operation parameters and influence the response of the beam in the presence of perturbations. Tunes close to integer numbers result in large *orbit amplification factors* making the dynamics particularly sensitive to perturbations. The fractional parts of SIRIUS nominal tunes are quite low, and increasing them would distance the tunes away from integer numbers, reducing the orbit amplification factors and improving orbit stability.

Changing the tunes can be achieved by actuating with the quadrupole magnets, but doing so takes the machine to a different working point, in which the DA can, and often is, smaller than the DA in nominal tunes. In different working points, thus, online optimization is essential for finding a new sextupole configuration to achieve a good DA and acceptable IE for operation.

In agreement with the experience in other facilities, it is shown in Chapter 4 that online optimization using RCDS can successfully improve the dynamics performance and lead to DA and IE improvements. This was observed for the SIRIUS storage ring both in the machine nominal tunes as well as in other working points, with higher tune fractional parts.

SIRIUS experience with online optimization is a valuable demonstration of this tool's efficiency in fourth-generation rings, specially because SIRIUS has more sextupole magnets families than MAX-IV, which, prior to this work, was the sole fourth-generation ring on which online optimization of nonlinear dynamics was carried out.

At the time of this writing, SIRIUS is operating with the sextupole configurations found during the experiments carried out while executing this project [20]. The configuration was found by online optimizing the machine with increased fractional tunes. The higher tunes indeed led to a reduction in orbit amplification factors and unprecedented orbit stability [10].

In the upcoming chapter, the dynamics of electrons in storage rings is examined.

The linear approximation theory is introduced, and nonlinear dynamics is treated as a perturbation. The goal is to introduce the optics functions and relevant quantities such as chromaticity and dispersion, and to present how a nonlinear dynamics is limited by the increase in instabilities and irregularities at large amplitudes. Chapter 2 provides a brief overview of optimization strategies and focuses on familiarizing the reader with the RCDS algorithm. Chapter 3 presents the methods, measurement procedures and diagnostics tools available and required for the execution of the online optimization experiments and Chapter 4 presents the results of the optimization at the SIRIUS storage ring.

CHAPTER 1

Theoretical background: single-particle dynamics

This chapter provides the theoretical knowledge on the dynamics of electrons in storage rings needed to acquaint the reader with the online optimization problem and the constraints involved. The main objective is to introduce the linear dynamics theory, the optics functions, the operation parameters such as the tunes and chromaticity and to conceptualize the amplitudes limitations due to the nonlinearities of the motion. This chapter also aims at introducing SIRIUS' operation parameters and specifications. We claim no original contribution. All the content presented here can be found in the accelerator physics and engineering literature, in particular, refs. [1, 11, 21, 22].

Despite the complicated physics of fully-coupled dynamics involving transverse, longitudinal and energy oscillations, damping and excitation of amplitudes, collective effects and instabilities, for the purpose of this dissertation and the optimization problem at sight, we model the motion of a single electron, focusing on the transverse dynamics at fixed energy, neglecting radiation losses and gains and any other collective interactions. These simplifications are justified for our immediate purposes because:

- the beam is injected into the storage ring on-energy: it has no significant energy deviations and thus it does not perform large energy and longitudinal oscillations once it is captured into the ring;

- radiation losses are only significant over a time scale of a couple of turns. Over this period, tens of transverse oscillations take place. A model neglecting losses is relatively accurate for a small number of turns soon after the injection;

- the linear and uncoupled dynamics this simpler modeling renders serves as an initial building block, which captures the hierarchically more important features of the dynamics and upon which elaborate modeling can be carried out, incorporating coupling, nonlinearities and perturbations, as well as collective effects;

In this simplified picture, the electron travels along the ring at the speed of light and executes transverse oscillations in two orthogonal planes. The dynamics takes place in a 4-dimensional phase space, identical to that of two independent quasi-periodic oscillators.

1.1 Motion of charged particles in magnetic fields

1.1.1 Circular cyclotron motion

An electron of charge e and momentum magnitude p follows a circular orbit of radius ρ when interacting with an uniform and time-independent magnetic field of magnitude B, directed perpendicularly to the orbit plane. In such conditions, the Lorentz force law predicts that the orbit radius reads

$$\rho = \frac{p}{Be}. \tag{1.1}$$

Rearranging this relation we can define a quantity with units of magnetic field × length which characterizes the momentum magnitude per unit charge of the beam, the *magnetic rigidity*:

$$R(p) \equiv B\rho = \frac{p}{e}. \tag{1.2}$$

1.1.2 Trajectory deflections
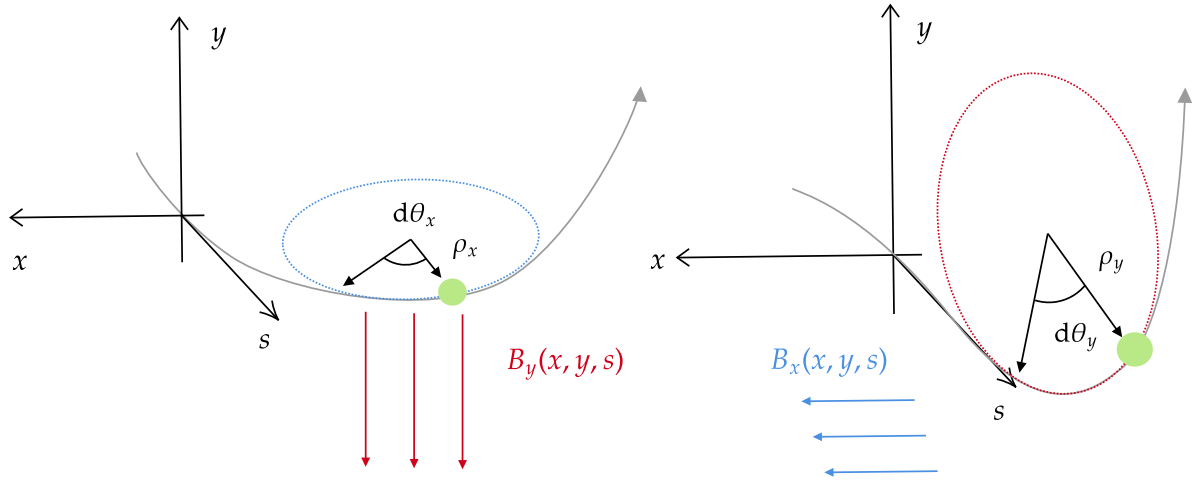
Figure 1.1: Illustration of trajectory deflection when interacting with magnetic fields.

Consider an electron traveling along a curve parameterized by the arc-length s with respect to an arbitrary reference point. Define the normal and bi-normal unit vectors so that we can identify a $x - y$ plane perpendicular to the motion. Let $B_x(x, y, s)$ and $B_y(x, y, s)$, denote the magnetic field components along the unit vectors. The interaction with the fields results in deflections of the trajectory, whose deflection angles $\mathrm{d}\theta_u$ in the $u = x, y$ plane can be estimated from the local curvature radius ρ_u and infinitesimal displacement $\mathrm{d}s$ with the aid of a local, instantaneous version of equation (1.1):

$$\mathrm{d}\theta_u = \frac{\mathrm{d}s}{\rho_u(s)} = \frac{e}{p} B_v(x, y, s)\mathrm{d}s = \frac{1}{R(p)} B_v(x, y, s)\mathrm{d}s, \quad u, v = x, y \quad \text{or} \quad y, x. \tag{1.3}$$

Where eq. (1.2) has been used to identify the p/e ratio as the magnetic rigidity $R(p)$. These considerations are illustrated in Fig. 1.1. The rigidity depends solely on the electron's momentum/energy and serves as the appropriate normalization constant to evaluate the instantaneous angular deflections in the electron's trajectory caused by magnetic fields.

1.2   The coordinate system for storage ring dynamics

As sketched by Fig. 2, electrons in a storage ring perform oscillations close to a nearly circular reference closed orbit. A convenient coordinate frame to describe the dynamics in this scenario can be constructed by imagining a reference particle traveling along a curve drawn by the tip of a vector $\mathbf{r}_0$, as Fig. 1.2 shows. This particle samples exactly the reference nominal orbit and travels a distance s along the ring, which can be used to parameterize the motion. The triad of direction vectors for the co-moving coordinate frame consists of the vector $\hat{\mathbf{s}}$, tangent to the trajectory, the vector $\hat{\mathbf{x}}$, normal to the trajectory, pointing in the direction at which $\hat{\mathbf{s}}$ changes, and a vector $\hat{\mathbf{y}} = \hat{\mathbf{x}} \times \hat{\mathbf{s}}$, bi-normal to the trajectory. This construction leads to a Frenet-Serret reference frame.

Assuming no curvature in the y plane, i.e. that the accelerator defines a curve whose plane is parallel to the facility flat floor, then the tangent, normal and binormal unit vectors defining the frame can be calculated as [21]

$$\hat{\mathbf{s}} = \frac{\mathrm{d}\mathbf{r}_0}{\mathrm{d}s}, \quad \hat{\mathbf{x}} = -\rho\frac{\mathrm{d}\hat{\mathbf{s}}}{\mathrm{d}s}, \quad \hat{\mathbf{y}} = \hat{\mathbf{x}} \times \hat{\mathbf{s}}, \tag{1.4}$$

where $\rho(s) = \|\mathrm{d}\hat{\mathbf{s}}/\mathrm{d}s\|^{-1}$ is the local curvature radius[1]. The vectors evolve along s as prescribed by the Frenet-Serret equations:

$$\frac{\mathrm{d}\hat{\mathbf{s}}}{\mathrm{d}s} = -\frac{1}{\rho(s)}\hat{\mathbf{x}}, \quad \frac{\mathrm{d}\hat{\mathbf{x}}}{\mathrm{d}s} = \frac{1}{\rho(s)}\hat{\mathbf{s}}, \quad \frac{\mathrm{d}\hat{\mathbf{y}}}{\mathrm{d}s} = 0. \tag{1.5}$$

The frame depends solely on the geometry of the specified path: the instantaneous curvature $\rho^{-1}(s)$. Since the curvature is defined by the strengths of the dipolar fields $B_0(s)$ in the y direction, then, eq. (1.3) leads to1. Theoretical background: single-particle dynamics

$$\frac{1}{\rho(s)} = \frac{B_0(s)}{R_0}, \tag{1.6}$$

where R_0 is the rigidity of the beam at the nominal energy.

The transverse deviations from the nominal orbit can be measured as projections along the unit vectors $\hat{\mathbf{x}}$, $\hat{\mathbf{y}}$ in the normal and bi-normal directions. These deviations characterize the transverse dynamics of the electron. One may also be concerned with the

---

[1]For a circular trajectory, $\mathbf{r}_0 = \begin{bmatrix} R\cos(s/R) & R\sin(s/R) & 0 \end{bmatrix}^\mathsf{T}$, $0 \leq s \leq L$, in the laboratory frame. So we can calculate $\hat{\mathbf{s}} = \begin{bmatrix} -\sin(s/R) & \cos(s/R) & 0 \end{bmatrix}^\mathsf{T}$, $\mathrm{d}\hat{\mathbf{s}}/\mathrm{d}s = -R^{-1}\begin{bmatrix} \cos(s/R) & \sin(s/R) & 0 \end{bmatrix}$, which reveals $\rho(s) = R$, justifying the interpretation of $\rho(s)$ as a curvature radius.

distance of a given particle from the reference particle along the curve. Such differences arise due to differences in the energy of the two particles. In the full, six-dimensional dynamics, the longitudinal distance from the reference particle and the energy deviations are conjugate dynamical variables characterizing the longitudinal dynamics. They typically oscillate within a range of stable values, characterizing the energy acceptance. As mentioned above, since no radiation loss nor gain will be considered in our modeling, the energy and longitudinal deviations from the reference particle shall be static and treated as fixed parameters.
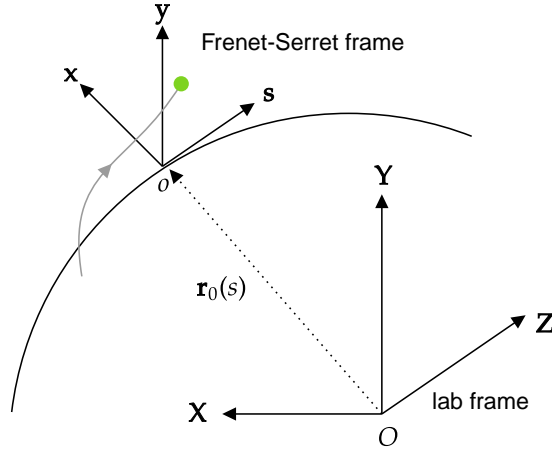
Figure 1.2: The Frenet-Serret coordinate system. Figure inspired by ref. [23].

1.3   Hamiltonian for the relativistic electron

To the derive equations of motion for the electron in a storage ring, the Lorentz equation in the Frenet-Serret frame could be further developed. However, a more formal, systematic and rigorous derivation can be obtained via the canonical formalism. The dynamics of relativistic electrons influenced by electromagnetic fields $(\Phi, \mathbf{A})$ is encapsulated by the Hamiltonian [24]

$$H = \sqrt{m^2 c^4 + (\mathbf{P} - e\mathbf{A})^2 c^2} + e\Phi,$$

e being the elementary charge and $\mathbf{P} = \mathbf{p} + e\mathbf{A}$ the canonical momentum, with $\mathbf{A}$ being the vector potential describing the magnetostatic fields of the lattice, i.e. $\mathbf{B} = \boldsymbol{\nabla} \times \mathbf{A}$. To obtain equations of motion for electrons in the storage ring, one usually follows the steps below:

- A canonical transformation to change coordinates is applied in order to describe the motion in terms of the Frenet-Serret frame variables x, y;

- Instead of time t, the Hamiltonian and the dynamical variables are described as functions of s, the longitudinal position along the ring;

- Paraxial approximation: the transverse momenta are assumed to be way smaller than the momentum along the trajectory's tangent direction. This allows the expansion of the square-root in the Hamiltonian as a power series, revealing the expression for an approximate Hamiltonian, which can be more easily handled;

- Geometric quantities are used: in the paraxial approximation, the canonical momenta for on-energy particles are identified with the derivatives with respect to the parameter s, i.e., $p_x = x' = \mathrm{d}x/\mathrm{d}s$ and $p_y = y' = \mathrm{d}y/\mathrm{d}s$, which represent the divergence angles from the nominal orbit. For off-energy particles, a correction factor is present;

All of the transformations and manipulations summarized above can be found in detail in the literature, such as in Refs. [1, 21, 22]. As mentioned previously, by neglecting RF cavities ($\Phi = 0$) and radiation losses, the energy will be a constant parameter, and the dynamics will consist solely of the transverse degrees of freedom. In this 4-dimensional dynamics, the set of canonical variables are (x, p_x, y, p_y), where the momenta are given by

$$p_x = x'(1 + \delta), \quad p_y = y'(1 + \delta) \tag{1.7}$$

and δ is the relative deviation from the nominal energy-momentum:

$$\delta \equiv \frac{P - P_0}{P_0} \approx \frac{E - E_0}{E_0}. \tag{1.8}$$

The ultra-relativistic approximation $E \approx pc$ was used. For on-energy particles, $p_x = x'$, $p_y = y'$.

Hamilton's equations for the paraxial-approximated Hamiltonian reveals the equations of motion for the x and y coordinates, which read:

$$x'' = -\frac{(1 + Gx)^2}{1 + \delta} \frac{B_y}{R_0} + G(1 + Gx), \quad y'' = \frac{(1 + Gx)^2}{1 + \delta} \frac{B_x}{R_0}, \tag{1.9}$$

where $R_0 = p_0/e$ is the magnetic rigidity of the beam at the nominal energy and $G(s) \equiv \rho^{-1}(s)$ is the inverse local radius of curvature, related to the dipole fields as in Eq. (1.6).

1.4 The magnetic fields

To study the motion, we need to specify the fields $B_x(s)$ and $B_y(s)$ acting on the beam. Since in a storage ring the magnets are arranged as periodic arrays of dipoles, quadrupole, and sextupoles, the $B_x(s)$ and $B_y(s)$ functions are periodic. The magnetic fields are sectionally defined and have the following functional forms

- Horizontal Dipole

$$B_x(s) = 0, \quad B_y(s) = B_0, \quad \text{inside dipoles}, \tag{1.10}$$

- Normal quadrupole

$$B_x = B_1 y, \quad B_y = B_1 x, \quad \text{inside quadrupoles}, \tag{1.11}$$

- Normal sextupole

$$B_x = B_2 xy, \quad B_y = \frac{1}{2} B_2 (x^2 - y^2), \quad \text{inside sextupoles}, \tag{1.12}$$

and zero everywhere else, in drift sections. Fields (1.10)–(1.12) are the so-called *normal multipole fields*, in contrast with *skew multipole fields*, which couple the horizontal and vertical dynamics. We will neglect skew fields and coupling for now. They can be treated as perturbations in perturbation theory schemes.

In eqs. (1.9), the magnetic rigidity normalizes all the fields. Thus, we define the normalized dipolar, quadrupolar and sextupolar field strengths, $G(s), K(s), S(s)$:

$$G(s) = \frac{B_0(s)}{R_0}, \quad K(s) = \frac{B_1(s)}{R_0}, \quad S(s) = \frac{B_2(s)}{R_0}. \tag{1.13}$$

For a SIRIUS superperiod, the functions are shown in Fig. 1.3. A superperiod consists of the basic repetition of four magnetic cells. SIRIUS has 5 superperiods. In other words, the curves in Fig. 1.3 repeat themselves five times along the 518 m of the ring. More details on the magnetic lattice are in section 3.1.

1.5 Linear dynamics

Expansion of eqs. (1.9) up to first order in the x, y, δ variables leads to [11]

$$x'' + (G^2 + K)x = G\delta, \quad y'' - Ky = 0. \tag{1.14}$$

For on-momentum particles, $\delta = 0$, both equations are instances of Hill's equations

$$u'' + K_u(s)u = 0, \tag{1.15}$$

i.e, a pair of parametric oscillators for $u = x, y$, with s-dependent and periodic focusing functions

$$K_x(s) = G^2(s) + K(s), \quad K_y(s) = -K(s),$$
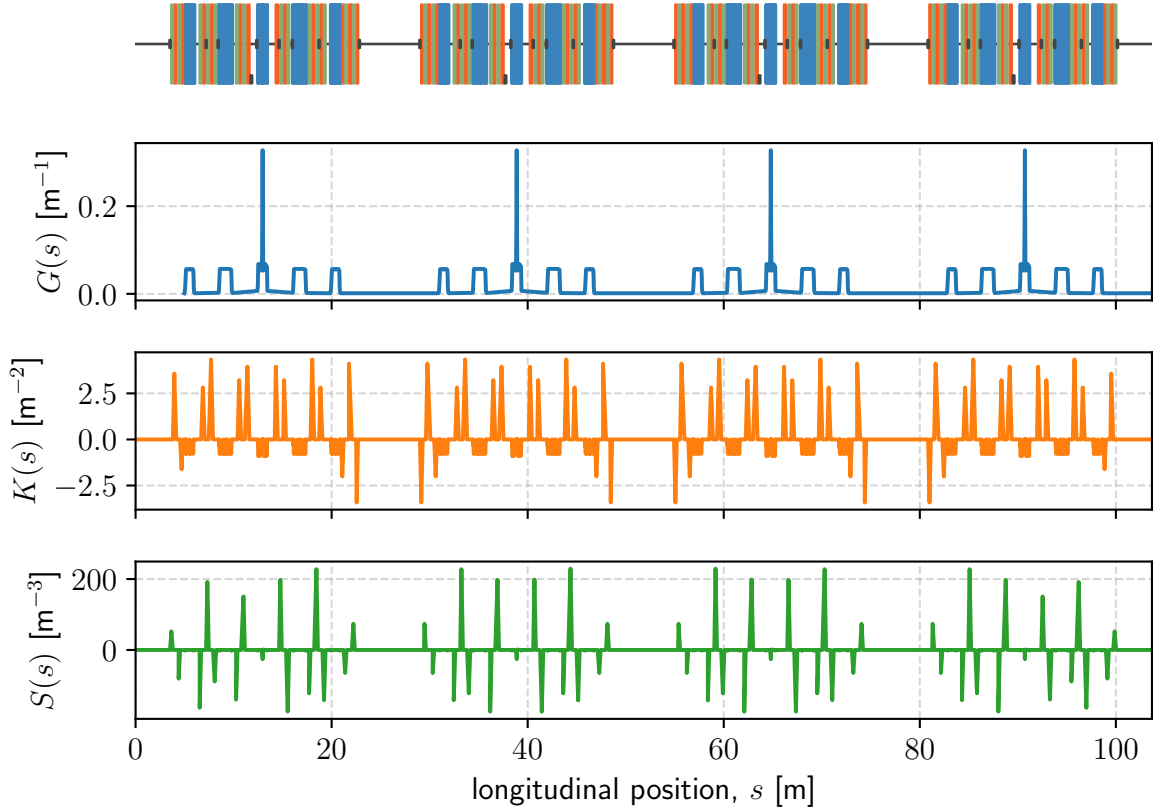
Figure 1.3: Normalized field functions for dipoles (top plot), quadrupoles (middle plot) and sextupoles (bottom plot) of a superperiod of SIRIUS lattice, shown at the top. Colored blocks represent the magnets of the accelerator lattice: blue for dipoles, orange for quadrupoles and green for sextupoles. The ring has a 5-fold symmetry, with the cells, fields, and optics function repeating the pattern shown above five times up to $s = 518$ m.

the analogs to an oscillator's spring force per unit mass. Motion in the linear approximation thus consists of oscillations around the closed orbit, known as *betatron oscillations*.

1.5.1 Pseudoharmonic description

Betatron motion can be cast in an amplitude-phase form. One can show that

$$u(s) = \sqrt{2\beta_u(s)J_u}\cos(\phi_u(s) + \phi_0), \quad u = x, y, \tag{1.16}$$

is a solution to (1.15), as long as the $\beta_u(s)$ function satisfies the boundary-value problem

$$\frac{1}{2}\beta_u'' + \beta_u K_u(s) - \frac{1}{\beta_u}\left(\frac{1}{4}\beta_u'^2 + 1\right) = 0, \quad \begin{cases} \beta_u(0) = \beta_u(L) \\ \beta_u'(0) = \beta_u'(L) \end{cases} \tag{1.17}$$

and the phase advance is given by

$$\phi_u(s) = \int_0^s \frac{1}{\beta_u(\sigma)} \mathrm{d}\sigma. \tag{1.18}$$

The motion is oscillatory, non-harmonic, and non-periodic. The oscillations envelope is the square root of the beta functions $\beta_u(s)$, which for the SIRIUS storage ring are shown in Fig. 1.4.
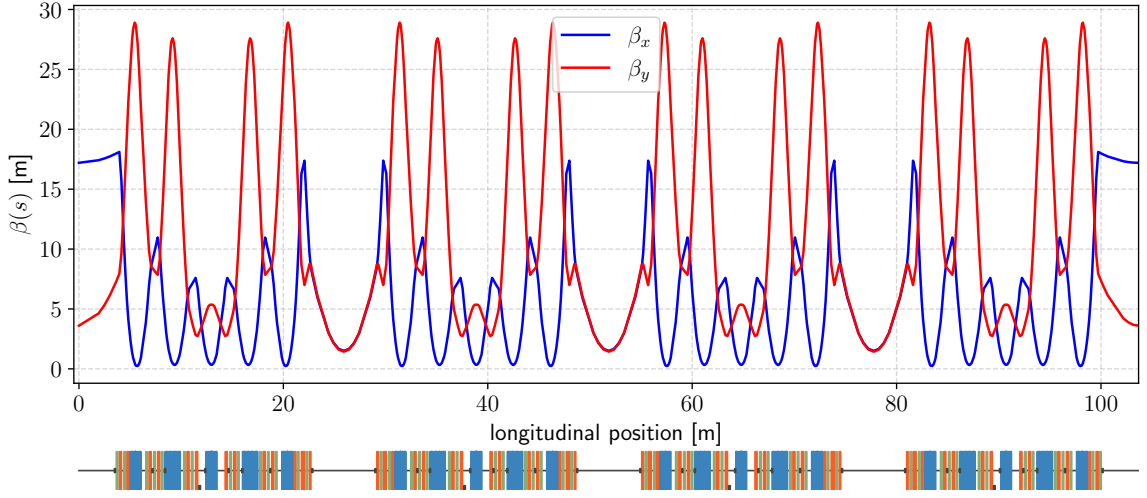
Figure 1.4: Betatron functions in a superperiod of the SIRIUS storage ring.

1.5.2 The tune

An important parameter of the dynamics is the *tune*: the phase advance over a revolution along the ring, in units of a complete cycle:

$$\nu_u = \frac{1}{2\pi} \int_s^{s+L} \frac{\mathrm{d}\sigma}{\beta_u(\sigma)} \equiv \frac{1}{2\pi} \oint \frac{\mathrm{d}s}{\beta_u(s)}.$$

The tune reveals the number of transverse oscillations per revolution along the ring. The optimized tunes during design phase for SIRIUS storage ring are $(\nu_x, \nu_y) = (49.08, 14.14)$. These were the machine tunes prior to this work.

When studying the effects of perturbations and nonlinearities acting on the beam, one realizes that tunes are global parameters in determining the beam's response. More specifically, the tunes impact over disturbances amplification factors, which are greatest when tunes are close to integer numbers. Ideally, it is desired for the tunes to be far from the integers, but also far from the half-integers. We examine the relation between the tunes and the effects of disturbances in more detail in section 1.6.2.

1.5.3   Turn-by-turn motion

If one keeps track of the time evolution of the u, u' variables at a fixed position along the ring, plotting them in a phase space, one realizes the quasi-periodic motion traces out ellipses. This fact can be analytically verified by calculating the derivative

$$u'(s) = -\sqrt{\frac{2J_u}{\beta_u}}\left[\sin(\phi_u(s) + \phi_0) - \frac{1}{2}\beta'_u(s)\cos(\phi_u(s) + \phi_0)\right], \qquad (1.19)$$

defining the functions $\alpha_u = -\frac{\beta'_u}{2}$ and $\gamma_u = \frac{(1+\alpha_u^2)}{\beta_u}$ and checking that u, u' satisfy the quadratic form

$$2J_u = \gamma_u u^2 + 2\alpha_u u u' + \beta_u u'^2, \qquad (1.20)$$

which describes the ellipse. The ellipse properties are determined by the $\beta_u(s), \alpha_u(s)$ and $\gamma_u(s)$ functions, also known as Courant-Snyder (C-S) parameters or Twiss parameters, as Fig. 1.5 shows. Since the parameters are functions of the position s, then, at each point along the accelerator, the Poincaré Section u, u' displays a different ellipse. Although different in shape, their areas are proportional to J_u, an invariant quantity determined by the particle's initial condition. The ellipse areas are thus conserved along the ring [1, 21].

Since the phase advance over a turn is $2\pi\nu + \phi_0$, the phase advance after the j-th turn is $2\pi\nu j + \phi_0$, and thus sampling the transverse motion at a fixed $s = s_0$ position reveals a harmonic displacement, which at the j-th turn reads

$$u_j(s_0) = \sqrt{2\beta_u(s_0)J_u}\cos(2\pi\nu_u j + \phi_u(s_0)). \qquad (1.21)$$

Knowledge of this formula allows the determination of the tunes (mod 2π) from the observation of Turn-by-Turn (TbT) motion of the beam. The time-series of positions can be fitted to eq. (1.21) in the time domain, or the signal can be processed in the frequency domain for the identification of the harmonic corresponding to ν_u.

1.6   Dispersive & chromatic effects and linear perturbations

1.6.1   Dispersion

The equation of motion for off-momentum particles in the horizontal plane, the first of eqs. (1.14), is a non-homogeneous Hill's equation. The solution consists of the linear combination of the homogeneous solution (betatron motion) and the particular solution: $x = x_\beta + x_\delta$, which represents an additional deviation from the nominal orbit. Since the non-homogeneous term, $G(s)\delta$, is proportional to δ, we can assume $x_\delta = \eta(s)\delta$, where $\eta(s)$ is the *dispersion function*. For this to be the solution, the dispersion should
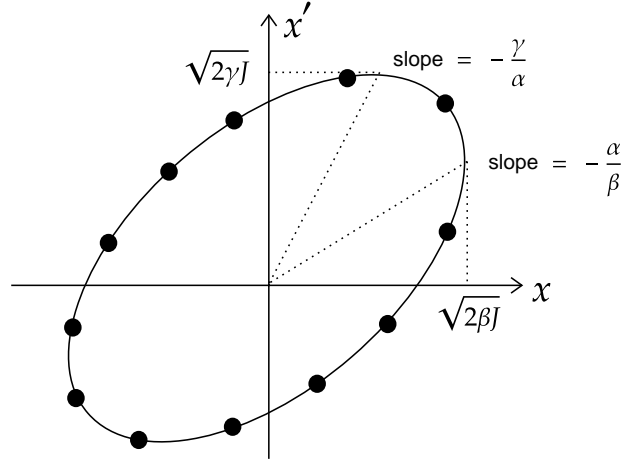
Figure 1.5: Ellipse traced by TbT motion in the (x, x') phase space. Optics functions $\alpha(s), \beta(s), \gamma(s)$ determine the principal axes aspect-ratio and the ellipse inclination at each longitudinal position along the ring. Figure inspired by ref. [22].

satisfy

$$\eta'' + (G^2 + K)\eta = G, \quad \begin{cases} \eta(0) = \eta(L), \\ \eta'(0) = \eta'(L). \end{cases}$$

The periodicity in the $\eta(s)$ function is required if we want to interpret it as a closed orbit distortion per relative momentum deviation. Thus, off-momentum particles perform betatron oscillations around a dispersive orbit, displaced from the nominal orbit by $\eta(s)\delta$. The dispersion function for the SIRIUS storage ring is shown in Fig. 1.6
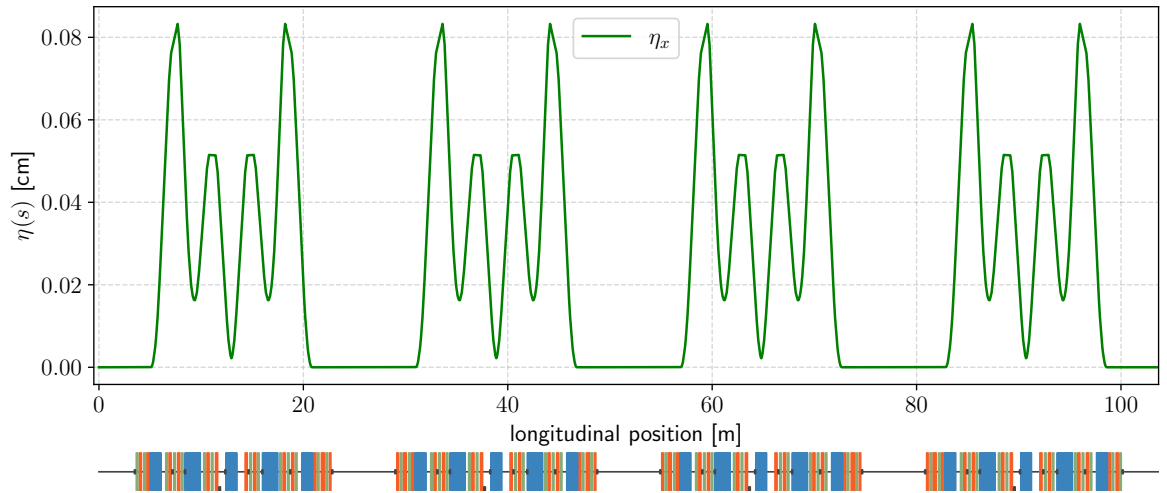
Figure 1.6: Dispersion function for a SIRIUS superperiod.

1.6.2   Linear Field Errors

In the presence of additional dipolar and quadrupolar fields representing field errors and deviations from the nominal fields, the orbit and focusing of the beam are changed. Assuming these are small perturbations and not sufficiently strong to perturb the beam severely, we can evaluate the disturbances to the unperturbed dynamics with a simple perturbation theory scheme. The details and derivations can be found in the literature, such as in chapter 2 of Ref. [21]. Here we highlight the main results.

Dipole errors

Suppose there are additional dipole fields $\Delta B_{0x}(s), \Delta B_{0y}(s)$ interacting with the beam other than the dipole fields of the nominal lattice. These translate into errors of the dipolar functions: $\Delta G_y(s) = -\Delta B_{0x}(s)/R_0$ and $\Delta G_x(s) = \Delta B_{0y}(s)/R_0$. In this scenario, the equations of motion read

$$x'' + K_x(s)x = G\delta + \Delta G_x(s), \quad y'' + K_y(s)y = \Delta G_y(s). \tag{1.22}$$

The solution consists of the combination of the betatron motion and the dispersive orbit (for the horizontal plane) plus the closed orbit distortion u_{co} induced by the additional bending terms due to the dipole errors. For a single thin bending error ΔG_u in the $u = x, y$ plane, acting for a length Δs around $s = s_0$, the closed orbit distortion u_{co} reads

$$u_{\text{co}}(s) = \frac{\sqrt{\beta_u(s)\beta_u(s_0)}}{2\sin \pi\nu_u} \Delta G_u \cos(\pi\nu_u - |\phi_u(s) - \phi_u(s_0)|)\Delta s. \tag{1.23}$$

For a distribution $\Delta G_u(s)$ of dipolar perturbations along the ring, we sum over the contributions:

$$u_{\text{co}}(s) = \frac{\sqrt{\beta_u(s)}}{2\sin \pi\nu_u} \int_s^{s+L} \Delta G_u(\sigma)\sqrt{\beta_u(\sigma)} \cos(\pi\nu_u + \phi_u(s) - \phi_u(\sigma)) \, \mathrm{d}\sigma. \tag{1.24}$$

The prefactor involving the sine of the tune shows how ν_u close to an integer can amplify the effects of the dipolar perturbations on orbit distortions. At first, aiming for tunes half-integer tunes $\nu = k/2, k \in \mathbb{Z}$ might seem desirable to minimize the distortions. Choosing so, however, increases the sensitivity to gradient errors, which we examine next.

Gradient errors

Gradient errors can be modeled as corrections to the focusing functions in the equations of motion: $K_u(s) \to K_u(s) + \Delta K_u(s)$, for $\Delta K_x(s) = \Delta B_{1y}(s)/R_0$ and $\Delta K_y(s) = -\Delta B_{1x}(s)/R_0$. The changes in beam focusing lead to changes in the beta-functions, phase advances and, consequently, the betatron tunes. One can show the

tune-shift as a consequence of a focusing gradient error ΔK_u, acting during a small longitudinal extent Δs around $s = s_0$ is [21]

$$\Delta \nu_u = \frac{1}{4\pi} \beta(s_0) \Delta K_u \Delta s.$$
(1.25)

Were we dealing with a defocusing error, a minus sign would preceed the above equation. For a distribution of errors we sum over the ring:

$$\Delta \nu = \frac{1}{4\pi} \oint \beta(s) \Delta K(s) \mathrm{d}s,$$
(1.26)

where the closed integration sign refers to a complete circulation along the ring, i.e., integration from s_0 to $s_0 + L$, for any $s_0 \in [0, L)$.

As for the induced error on the beta-functions, it is possible to show that the relative error, known as beta-beat, can be expressed as

$$\frac{\Delta \beta_u(s)}{\beta_u(s)} = -\frac{1}{2\sin(2\pi\nu_u)} \int_s^{s+L} \beta(\sigma) \Delta K_u(\sigma) \cos[2(\phi_u(\sigma) - \phi_u(s) - \pi\nu)] \mathrm{d}\sigma.$$
(1.27)

which is the largest for $2\nu_u$ closest to an integer. This means we must avoid tunes close to half-integers if we want to avoid the coherent build-up of betatron amplitudes, which can eventually lead to beam loss. Integer or half-integer tunes are the simplest instances of resonances the beam can be subject to. A more general overview of resonances is presented in subsection 1.7.3.

1.6.3 Chromaticity

We have seen how the bending angles at the dipoles are different for electrons with different energies. This is the origin of dispersive orbits. However, energy deviations affect not only the closed orbit by means of the dispersion effect, but also the focusing of the trajectories, since a more/less energetic beam has higher/lower rigidity and thus is focused differently when passing through gradient fields.

Expansion of the equations of motion, eqs. (1.9), for off-energy particles up to the order of terms $u\delta$ (for $u = x, y$) reveals additional higher-order gradient errors. The focusing functions are corrected by $K_u(s) \to K_u(s) + \Delta K_u(s)$ [21, 23], where

$$\Delta K_x = -(K + 2G^2)\delta \approx -K_x \delta$$
(1.28)

$$\Delta K_y = K\delta = -K_y\delta$$
(1.29)

This means there exists an energy-dependent tune-shift effect caused by the gradient error.

Using eq. (1.26), the tune-shift reads

$$\Delta\nu_u = -\frac{1}{4\pi} \oint \beta_u K_u \delta \, \mathrm{d}s \,, \tag{1.30}$$

for the $u = x, y$ planes. We can define the *linear chromaticity* in the $u = x, y$ direction as tune-shift $\Delta\nu_u$ per relative energy deviation δ:

$$\xi_u = \frac{\mathrm{d}\nu_u}{\mathrm{d}\delta}. \tag{1.31}$$

The chromaticity created by the linear lattice is also called natural chromaticity. Using expression (1.30) for the tune-shift, the natural chromaticity reads

$$\xi_{u,\mathrm{nat}} = -\frac{1}{4\pi} \oint K_u \beta_u \, \mathrm{d}s \,. \tag{1.32}$$

This chromatic aberration effect needs to be corrected to guarantee energy-independent focusing. Correction can be attained with the insertion of sextupolar fields, specifically in the dispersive sections of the storage ring. In such regions, off-energy particles follow a dispersive orbit, and their position reads $x(s) = x_\beta(s) + \eta(s)\delta$, where $x_\beta(s)$ consists on the betatron oscillations. Since sextupolar fields are of the form

$$B_x = B_2 xy, \quad B_y = \frac{B_2}{2}(x^2 - y^2),$$

then, the off-momentum particles "see" the fields

$$B_x = B_2(x_\beta y + \eta\delta y), \quad B_y = \frac{B_2}{2}(x_\beta^2 - y^2) + B_2 x_\beta \eta\delta + \frac{B_2}{2}(\eta\delta)^2.$$

So, to lowest order in eqs. (1.9), they feel a dipolar perturbation (which contributes to orbit distortions) and the following gradient perturbation:

$$\Delta K_{x,y}(\delta) = \pm S\eta\delta,$$

recalling that $S(s) = B_2/R_0$.

Considering the contributions from both the errors induced by energy deviations and also the lowest order sextupole gradient effect, we have a gradient shift of $\Delta K_u = -(K_u \mp S\eta)\delta$ to be inserted in eq. (1.26). The chromaticity in a lattice with sextupoles thus reads

$$\xi_u = -\frac{1}{4\pi} \oint \beta_u(K_u \mp S\eta) \, \mathrm{d}s \,, \tag{1.33}$$

with the minus sign for $u = x$ and the plus sign for $u = y$.

Formula (1.33) reveals that chromaticity depends linearly on sextupole strengths. This allows for its correction and tuning to desired values. In the SIRIUS storage ring, the
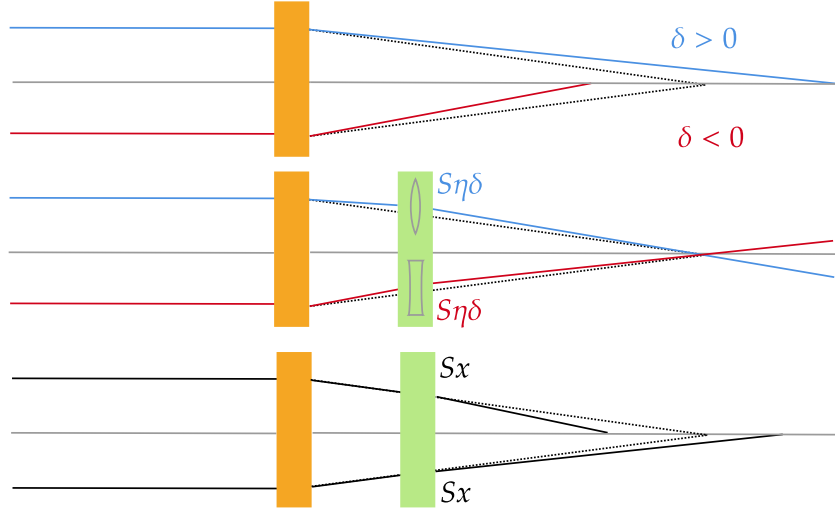
Figure 1.7: Illustration of chromatic aberrations (top), their correction with sextupoles (middle) and examples of geometric aberrations (bottom).

operation chromaticity of about $+2.5$ for each plane was determined with the objective of mitigating the transverse instabilities induced by the resistive-wall effect in the range of currents the storage ring is expected to operate: 100 to 350 mA [25, section 7.3].

Since a focusing sextupole field focuses in a given plane and defocuses in the other, at least two sextupole families are required for chromaticity correction. To optimize the sextupole strengths required for correction, one family must be placed where $\beta_x > \beta_y$ and another where $\beta_y < \beta_x$. The cost of correcting chromaticity with sextupole is the insertion of nonlinearities in the dynamics. If on the one-hand, amplitude-dependent focusing is needed to correct the energy-dependent focusing (chromaticity), on the other hand it also influence particles with large amplitudes with nonlinearities. To allow for more control over the nonlinear effects and optimization of the dynamics, some families of sextupoles are also placed in non-dispersive sections. They are called achromatic families, since they have no effect over chromaticity up to leading order.

1.7 Nonlinear dynamics, perturbations, resonances and tune-shifts

The fields of sextupoles make the dynamics intrinsically nonlinear. To understand the effects of nonlinearities in a generic manner, we develop a basic Hamiltonian perturbation theory in the upcoming sections. However, this requires us to step back momentarily to review linear dynamics in the action-angle variables formalism, upon which we proceed with canonical perturbation theory.

1.7.1 Action-Angle Variables

The betatron equations of motion, Eqs. (1.15), can be obtained as Hamilton's equations for an effective, linear Hamiltonian

$$\mathcal{H}_u = \frac{1}{2}u'^2 + \frac{1}{2}K_u(s)u^2, \tag{1.34}$$

summed over $u = x, y$. A transformation $(u, u') \to (\psi_u, J_u)$ to Action-angle variables is implicitly implemented by the type–1 generating function [21]

$$F_1(u, \phi_u) = \int u' \, \mathrm{d}u = -\frac{u^2}{2\beta_u}\left(\tan \phi_u - \frac{\beta'_u}{2}\right). \tag{1.35}$$

The action variable reads

$$J_u = -\frac{\partial F_1}{\partial \phi_u} = \frac{u^2}{2\beta_u}\sec^2 \phi_u = \frac{1}{2\beta_u}[u^2 + (\beta_u u' + \alpha_u u^2)], \tag{1.36}$$

from which we can recover the pseudo-harmonic form $u = \sqrt{2\beta_u J_u}\cos(\phi_u(s) + \phi_0)$, and identify the constant J we met before as the action and the betatron phase advance as the angle variable.

In the J, ϕ variables, the new Hamiltonian is $H_0(\phi, J)$, given by

$$H_u = \mathcal{H}_u + \frac{\partial F_1}{\partial s} = \frac{J_u}{\beta_u}. \tag{1.37}$$

Performing the change to action-angle variables in both the horizontal and vertical planes, we find the action-angle Hamiltonian for 4D dynamics:

$$H_0 = \frac{J_x}{\beta_x} + \frac{J_y}{\beta_y}. \tag{1.38}$$

Hamilton's equations read

$$\phi'_u = \frac{1}{\beta_u(s)}, \qquad J'_u = 0. \tag{1.39}$$

1.7.2 Perturbations and tune-shifts

Linear motion is integrable since it can be written in terms of the action variable only (angle-independent Hamiltonian). This means the action variable is a constant of motion.

Linear motion, though, is only a useful first approximation. In reality, in a storage ring, there are higher-order multipole magnets, such as sextupole magnets, and also multipole, alignment and excitation errors acting as perturbations. Generically referring
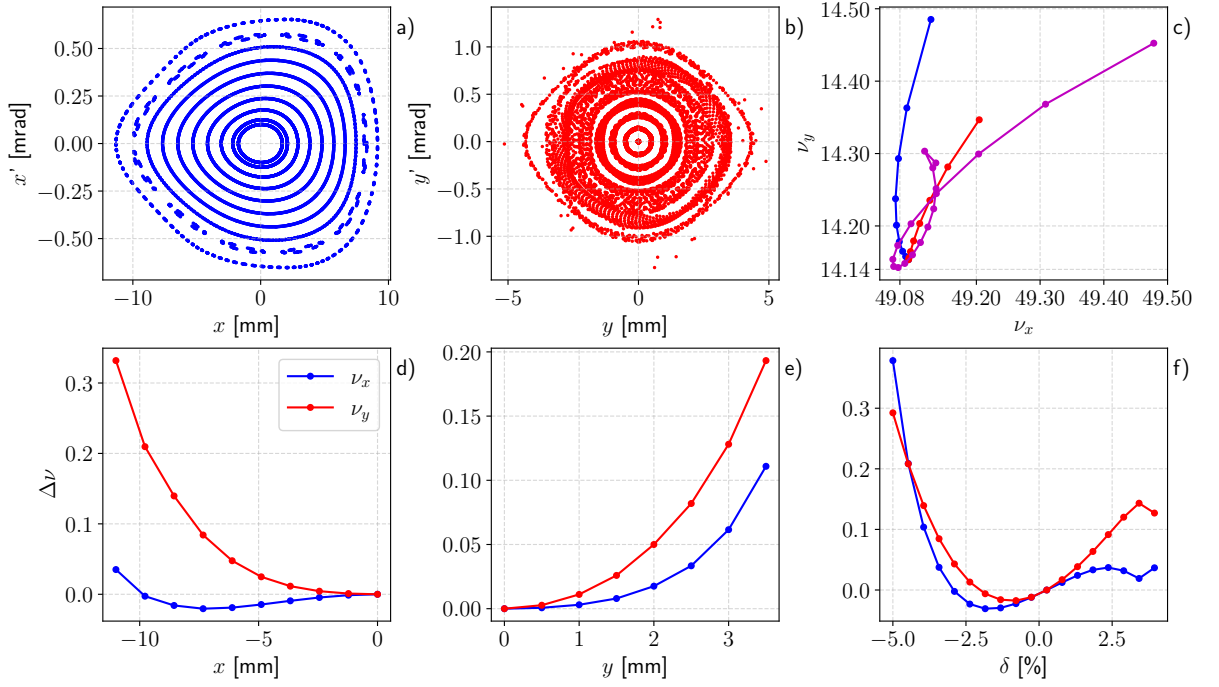
Figure 1.8: Illustration of main characteristics in nonlinear dynamics. a) & b): Poincaré sections for motion with increasing horizontal & vertical amplitudes, respectively; c) Path traced in tune-space for each ellipse of a) in blue, for b) in red, and for each δ in f), in purple. d) & e): x and y amplitude-dependent tune-shifts for each ellipse of a) & b), respectively; f) energy-dependent tune-shifts

to perturbations as the potential $V(J, \phi)$, we can write the perturbed Hamiltonian

$$H(J, \phi) = H_0 + V(J, \phi), \tag{1.40}$$

For which Hamilton's equations read

$$\phi'_u = \frac{1}{\beta_u(s)} + \frac{\partial V(J, \phi)}{\partial J_u}, \quad J'_u = -\frac{\partial V(J, \phi)}{\partial \phi_u}. \tag{1.41}$$

The action is no longer an invariant. It changes as prescribed by the rate of change of the potential with respect to the phase. The phase also changes. The phase advance rate deviates from the linear betatron phase advance, which translates directly into tune-shifts. In this scenario, the tunes depend not only on the momentum, via the chromaticity, but also on the amplitudes (actions). In a general form, we can be express the tunes as

$$\nu_u = \nu_{u0} + \xi_u(\delta)\delta + \alpha_{uu}J_u + \alpha_{uv}J_v, \tag{1.42}$$

where ξ_u represents the energy-dependent tune-shifts (higher-order generalization of the linear chromaticity), and the other components consist on the amplitude-dependent tune-shifts, up to first order in the actions.

Figure 1.8 highlights the main characteristics of the nonlinear dynamics. In a) and b) particles are simulated in SIRIUS' computer model with increasingly larger initial

amplitudes in the x and y planes, respectively. The large-amplitude ellipses are distorted, since the action J is no longer an integral of motion. Some large-amplitude particles do not survive. In d) and e), the deviations in horizontal and vertical tunes are shown for the a) and b) simulations, respectively. In d), the tune-shifts in the y and x planes are shown for each initial x amplitude. In e), the tune-shifts for each initial y amplitude in b) is shown. These plots outline the distortion of phase space ellipses, the existence of limiting amplitudes under which regular motion occurs, and the dependence of the tunes with the amplitudes.

In plot e) of Fig. 1.8, the chromatic (energy-dependent) tune-shifts are shown: the tune-shifts of particle simulated with energy deviations in the range of -5% to 5%. Linear chromaticity is the derivative of this curve around $\delta = 0$. In c), the blue curve represents the path traced in tune-space as the x amplitude increase, i.e., the tunes for each initial condition of the simulations in a); the red curve represents the path traced as the y amplitudes increase, i.e., the tunes for each initial condition of the simulations in b). The purple curve is the path traced for each δ in the simulations shown at f).

1.7.3 Resonances

4D linear unperturbed motion consists of the motion of two uncoupled parametric oscillators. As a quasi-periodic integrable system, the phase-space is diffeomorphic to the 2-Torus, $\mathbb{T}^2$, and there are an infinite number of such tori covering phase space, corresponding to the different choices of initial conditions J_u.

Canonical perturbation theory applied to perturbed motion fails to converge whenever the ratio of tunes is sufficiently rational (resonant tori). The Poincare-Birkhoff theorem states that under such conditions, almost all the periodic phase-space orbits disappear, i.e., almost all the tori are destroyed. An even number of tori survive, half stable and half unstable [26, section 10.2]. Unstable motion in a storage ring eventually leads to beam loss.

The condition for sufficiently rational tunes, i.e, resonant tori, can be expressed as

$$m\nu_x + n\nu_y = \ell, \tag{1.43}$$

for $n, m, \ell \in \mathbb{Z}$. This condition defines lines in tune-space corresponding to the locus in which perturbation theory fails and motion can become unstable: resonance lines.

We say $|n| + |m|$ is the order of the resonance, which is related to the order of the multipole field perturbation from which it arises. Resonances arising from linear field errors, already anticipated in section 1.6.2, are those described by $\nu_x = \ell$ or $\nu_y = \ell, \ell \in \mathbb{Z}$. Normal gradient field errors drive $2\nu_x = \ell$ or $2\nu_y = \ell$ resonances. Skew gradients couple both planes and can drive the famous sum and difference resonances $\nu_x + \nu_y = \ell, \nu_x - \nu_y = \ell$. Sextupoles, up to first-order in perturbation theory, can drive the $3\nu_x = \ell$, resonance,

as well as $nu_x \pm 2\nu_y = \ell$ and $\nu_x = \ell$ resonances [22, section 11.2.4]. Figure 1.9 depicts resonance lines in tune-space for resonances up to second, third and fourth order, in the left, middle and right plots, respectively.
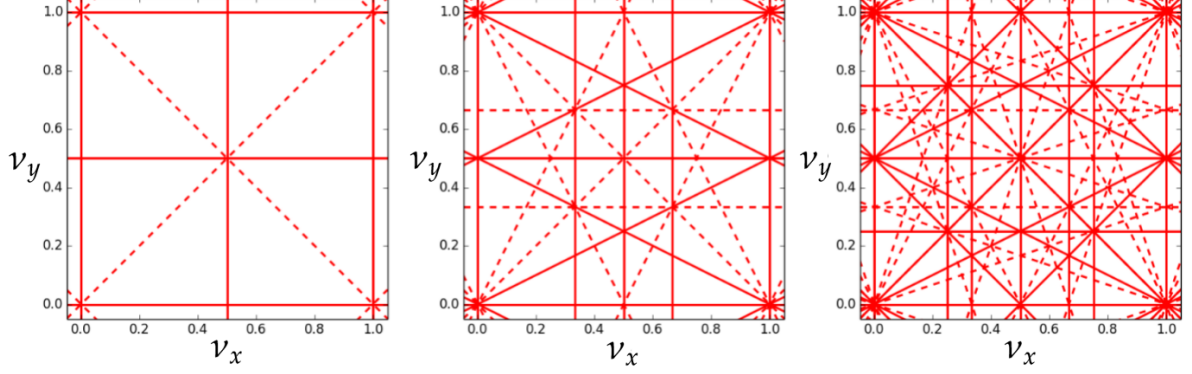
Figure 1.9: Resonance lines in tune space up to 2nd, 3rd and 4th order, respectively. Solid lines correspond to resonances driven by normal multipole fields, while dashed lines correspond to resonances driven by skew multipole fields. Figure adapted from ref. [27]

1.7.4 The Dynamic Aperture

The stability of nonlinear dynamics can become sensitive when amplitudes are large. In this scenario, the effects of the nonlinear fields become more significant and the perturbations are dialed up, breaking down the stable tori. Even low-amplitude motion can be dangerous in the long-term due to the phenomenon of Arnold diffusion [22, 28]: because of the tune-shifts, especially the amplitude-dependent tune shifts, the tunes can wander in tune space and eventually cross resonance conditions.

Despite the complexity of predicting stability of nonlinear perturbed dynamics, in electron storage rings, we usually observe the existence of an amplitude limit beyond which instabilities increase and the particles are lost, while the particles below the limiting amplitudes survive. In other words, there are limitations to the maximum transverse amplitudes displaying regular and bounded motion. This behavior was anticipated by the simulations shown in plots a) and b) of Fig. 1.8 and is also verified in the actual machine during experiments.

The border of the region of stability is the *dynamic aperture* (DA). This term can be used to refer to the limiting amplitudes in any of the dynamical variables of phase-space. In this work, we are mostly concerned with the DA in the (x, x') phase space because of its importance during the beam injection for accumulation into the storage ring.

During injection, if the horizontal amplitudes are larger than the DA along x or x', the beam is not captured efficiently into the storage ring. In this case, increasing the DA to accommodate the incoming beam would be interesting, which is exactly what

we aimed at while developing this project.

Since the DA is determined by the nonlinear perturbations, it is possible that tuning the nonlinear fields in a particular manner can render an optimum configuration with increased DA. In the upcoming chapter, this idea is developed in more detail.

CHAPTER 2

Online Optimization

This chapter defines, introduces and justifies online optimization of synchrotron storage rings nonlinear dynamics. The Robust Conjugate Direction Search (RCDS) algorithm is introduced, as well as the other optimization routines from which it was built upon. This chapter adds no novelty to the literature in optimization. It is an overview for merely pedagogic purposes. It mostly draws from the discussion presented by Numerical Recipes, ref. [29], as well as chapters 7 and 8 of ref. [23] and ref. [15].

2.1 Defining Online Optimization

Consider a system that possesses some sort of figure of merit which depends on the collective state of a set of relevant components, parts, or operation modes which constitute the parameters or decision variables. There is no mechanistic/deterministic or probabilistic model for the dependence of the figure of merit on the parameters' state, but it is well known that the parameters affect the figure of merit. One may call the relevant parameters knobs, since they can be used to tune the figure of merit.

Now suppose one wants to tune the knobs so the figure of merit reaches a certain value, or so that it is minimized or maximized. This is an optimization problem, with the figure of merit being the objective function. Since the whole system is a black-box, to measure different values for the objective function, i.e., to sample it, the knobs must be varied and the objective function must be measured, a process that may be expensive. The tuning procedure thus consists on trial-and-error iterations of changing the knobs, evaluating the objection and judging the quality of the changes performed.

A computer-automated routine or algorithm employing some strategy to seek the desired value or extremum of the objective function while the machine functioning is what we define as online optimization. The program must measure the objective function, read the current state of the knobs, calculate or decide and apply the changes to the knobs, measure the objective again and evaluate the quality of the changes over the objective. It incorporates this information when making the decision on how much to change the knobs next. The process is iterated until the desired outcome is reached.

The Dynamic Aperture (DA) optimization problem suits this heuristic, black-

box optimization scheme very well. The DA is a figure of merit related to the nonlinear dynamics–in SIRIUS' case, the sextupole magnets. There is no analytical/statistical model predicting DA changes given sextupole nudges so the problem cannot be inverted to tune the sextupoles to render the DA a desired value. The tuning procedure must be based on trial-and-error.

2.2 Justifying Online Optimization

2.2.1 Why not correct the nonlinear optics?

Several well-established and effective correction schemes exist for managing linear dynamics in storage rings. These methods rely on measurable figures of merit, enabling diagnostics of linear dynamics and optics. Crucially, they leverage linearly controllable adjustment knobs, allowing for the inversion of the problem—determining how much to tune the knobs to achieve a specific figure of merit. Examples include the widely used Linear Optics from Closed Orbits (LOCO) method, as originally introduced in ref. [30] and routinely applied to SIRIUS [31, 32], and other methods utilizing turn-by-turn data evaluation [23, chapter 5]. These correction schemes ensure that linear optics parameters, dependent on dipoles and quadrupoles, such as optics functions, meet specifications.

Recently, LOCO-inspired schemes have been extended to encompass nonlinear magnets and correct nonlinear optics. These methods have proven successful in addressing the state of sextupoles and octupoles, reportedly enhancing the DA and beam lifetime at the MAX-IV, [33] and NSLS-II [34] machines. These sophisticated procedures rely on a bottom-up understanding of how off-energy orbits appear for a specific configuration of nonlinear magnets.

Despite the value of these approaches, this master's project adopts the pragmatic, heuristic online optimization strategy. This choice is driven by the immediate need to optimize DA performance for the top-up operation mode and the considerations of available time and task complexity aligning with a master's degree scope. We acknowledge the significance of theory-based correction schemes as crucial next steps for comprehending the machine and establishing connections with the machine computer model, a pursuit to be completed in the near future.

2.2.2 The logic of nonlinear dynamics online optimization

During the design phase of SIRIUS, the strengths of the sextupole families and symmetry of the nonlinear magnetic lattice were determined through a comprehensive multi-objective optimization process. This process aimed to identify the lattice configuration that statistically would yield the highest DA and optimal lifetime performance based on particle tracking simulations with different lattice error configurations [13]. The most

successful and feasible solution (lattice) resulting from these simulation-based optimization studies was subsequently implemented in the actual machine during the commissioning phase.

The optimization work accounted for the presence of expected errors arising from magnet misalignments or deviations in magnetic fields. These errors introduce additional perturbations that can degrade the DA and were intentionally introduced into the model during the simulations for evaluating the figures of merit more realistically. Multiple machine models, each with different error configurations distributed across various magnets, were generated. The lattices derived from these models were then evaluated through simulations. The best lattice, determined based on average performance across various error configurations, demonstrated the highest average DA and average lifetime in tracking simulations.

In the actual machine, a specific configuration of errors becomes a reality, resulting in a distinct physical magnetic lattice. For this particular lattice, the optimized configuration identified during simulations in the design phase may not necessarily be the one that yields the largest DA or optimal lifetime. However, it is anticipated that optimum sextupole configuration for the realized lattice is not significantly different from the reference configuration chosen and implemented in the machine. Essentially, the assumption is that errors are small and the online optimization procedure, therefore, involves a mere fine-tuning of the strengths of the sextupole lattice to achieve its best-performing configuration, compensating for nonlinear dynamics perturbations and small residual perturbations from linear dynamics. In other words, online optimization consists on tailoring the sextupole strengths to match the realized lattice.

2.3   Robust Conjugate Direction Search Algorithm

Optimization routines and algorithms are commonly categorized based on whether they involve the calculation of derivatives (gradient-based) or rely solely on the comparison of objective function values (gradient-free). The latter can be further classified into direct- or indirect-search methods, depending on whether the extremum search relies on direct comparisons of the objective function or on a mathematical model of it, respectively [29].

Both gradient-based and gradient-free strategies rely on the comparison of the objective function at different points of the parameter space. If the objective function suffers with noise, it can significantly reduce the efficiency of the optimization routine [23, 29]. In Chap. 7, section 7.3.1 of Ref. [23], a review of traditional optimization algorithms (e.g. gradient descent, Nelder-Mead simplex method, Powell method) shows how most of them suffer to find minima to, at least, the precision of the noise σ the objective function is subjected to.

The Robust Conjugate Direction Search (RCDS) algorithm is an indirect-search, gradient-free optimization algorithm introduced in Ref. [15]. The algorithm comprises a main loop for constructing and managing optimal search directions along the knobs space (Powell's Method) and a one-dimensional optimizer responsible for a noise-aware search for the minimum along a given direction. Demonstrated in ref. [15] and [23, section 7.3.3], the algorithm can optimize the objective function with a precision at least equivalent to the objective-function noise, being suitable for online optimization problems. Specifically, for accelerator applications, the algorithm has been successfully applied to optimize beam steering and optics matching during injection [15], reduce horizontal emittance [15, 16], and optimize dynamic aperture [15–19] at machines such as SPEAR3, NSLS-II, MAX-IV, and ESRF. It has become a standard tool for optimizing the DA.

To this date, the only 4th-generation machine RCDS has been applied to was MAX-IV. The machine has five sextupole families and five octupole families. Selecting combinations of these families, subject to relevant operation constraints, such as keeping chromaticity unchanged, resulted in a 6-dimensional parameter search space [18]. SIRIUS, on the other hand, has 21-sextupole families. The application of RCDS in a 4GSR with a larger search space is of great interest to the community, especially for upcoming upgrades and new 4GSR projects currently under construction.

2.3.1   One-dimensional optimizers

RCDS' distinct noise robustness is due to the cumulative effect of minor modifications of well-known indirect-search routines. To grasp how it works, a brief overview on its predecessors is presented next.

Bracketing the minimum

Let $f(x) \in \mathbb{R}$ be the objective function depending on the single knob $x \in \mathbb{R}$. The goal of optimizing f is accomplished through a search over its domain. Since maximizing f is equivalent to minimizing $-f$, in the following discussion we shall refer to minimization only. The search for the minimum is usually preceded by initially *bracketing* the minimum. We seek points $a < b < c$ in the domain such that $f(b)$ is smaller than both $f(a)$ and $f(c)$. If f is reasonably smooth, we can be certain there will be a minimum in the interval (a, c). Standard bracket routines for well-behaved, noiseless objective functions can be found in the literature [29, section 10.1]. They mostly consist on starting from an initial point, scanning the line "downhill", i.e., as long as it decreases. The scanning stops when f stops decreasing. This allows identifying a first guess for the minimum, $x = b$, as well as $x = a$ and $x = c$, the borders the brackets. The bracketing procedure can be seen as a coarse-grained scan performed initially.

Line scan

After bracketing, the minimum is then more finely searched by a routine referred to as line search or line scan. The most common line search methods are the *golden section search* and *parabolic interpolation* [29, sections 10.2 and 10.3]. Parabolic Interpolation is an indirect-search method. A parabola is fitted to the values $f(a), f(b), f(c)$ the function takes in the brackets. The parabola vertex then gives the estimate for f's minimum. Both of these methods rely on comparisons of the objective function at different points in the parameter space. They assume that the objective function f is deterministic and they trust their observed behavior. In other words, they are completely unaware of any experimental noise in the system. In what follows, we assume what we actually measure in the control-room is $f(x) + \xi$, where $\xi \sim \mathcal{N}(\mu = 0, \sigma)$ is a random variable modeling the experimental noise, with σ being expected noise error, $\sigma^2 = \text{Var}[\xi]$.

RCDS bracketing

For the optimization of noisy objective functions, the line optimizer introduced in ref. [15] incorporates minor modifications to the traditional bracketing and parabolic interpolation line scan routines. Unlike traditional bracketing, RCDS enforces the stricter condition for accepting a and c as the brackets' borders. It demands that $f(b) + 3\sigma < f(a)$ and $f(b) + 3\sigma < f(c)$, where σ is the standard deviation of the objective function values, its experimental noise. In other words, RCDS brackets are obtained by scanning f downhill not only until the function stops decreasing, but until it departs from the best guess for the minimum by at least three times the expected error. This increases the likelihood that the observed trend represents real behavior of the objective function rather than noise. Pseudocode for a simple RCDS bracketing routine is presented in Algorithm 1 of Appendix A.

Figure 2.1 illustrates the RCDS bracketing. Starting from x_0, taken as the first guess for the minimum, $f(x_1)$ is measured. Since it is no grater than $f(x_0) + 3\sigma$, the scan continues up to x_2, which is updated as the the minimum. When measuring $f(x_3)$, condition $f(x_3) > f(x_2) + 3\sigma$ is true and the scanning in the positive direction stops. The starting point, x_0, is checked for the condition $f(x_0) > f(x_3) + 3\sigma$. If true, as in fig. 2.1, there is no need to scan in the negative direction and the brackets will be (x_0, x_2, x_3). If the condition is false, the scanning continues in the negative direction until x^* satisfying $f(x^*) > f(x_3) + 3\sigma$ is found, giving (x^*, x_2, x_3) as the bracket.

RCDS line scan

Next, for the line scan, a parabola is fitted within the brackets using the points previously sampled during the bracketing. The parabola vertex is taken as the objective function minimum. Prior to fitting, however, an outlier verification routine scans the
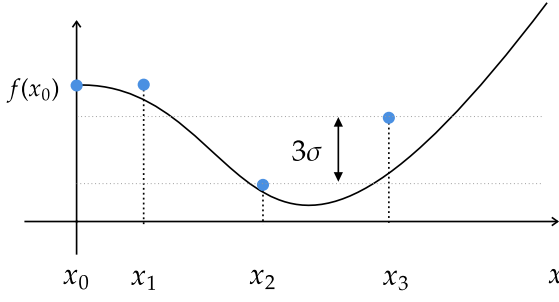
Figure 2.1: Illustration of RCDS bracketing. Black curve is the objective function, blue dots are its measurements, with noise. Bracketing routine: scan the objective function downhill, updating the guess for the minimum, until f stops decreasing and increases by more than 3σ compared the minimum.
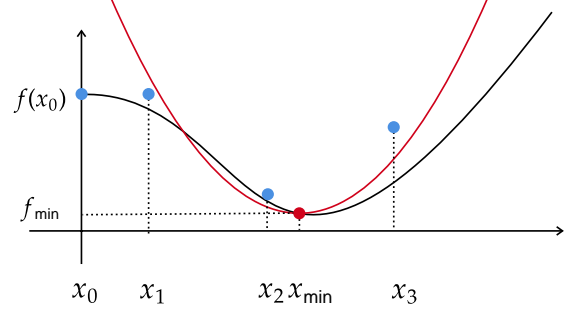
Figure 2.2: Illustration of RCDS line scan procedure: perform a parabolic fitting (red curve) over a curated set of objective function measurements (blue dots) within the brackets. Outliers are removed, if any is present. The parabola vertex is the best guess for f's minimum.

measured values of f during bracketing. If any point is identified as an outlier, according the routine described in Appendix A, it is discarded, and the fitting process is repeated without it, as long as a sufficient number (specified by the user) of measured values of f is still available. If that is not the case, additional measurements of f are carried out prior to fitting.

2.3.2   Powell's method

How could we optimize an objective function $f(\mathbf{x}) \in \mathbb{R}$ depending on the set of p parameters $\{x_i\}_{i=1,\dots,p}$? The simplest idea is to iteratively nudge each knob individually: optimize f by changing x_1, while the other knobs remain fixed, then optimize by changing x_2 only, and so forth. In other words, since each one of the knobs defines a direction whose basis vector is $\hat{\mathbf{e}}_i$, we could scan each direction, one at once, using the noise-robust line-optimizer introduced in the previous section.

Formally, we are reducing a multi-dimensional optimization problem into a series of 1-dimensional searches. That is, given an initial configuration of the parameters (an initial position) $\mathbf{x}_0$, and a direction $\hat{\mathbf{n}}$, we have the one-dimensional problem to minimize $g(\delta) = f(\mathbf{x}_0 + \delta\hat{\mathbf{n}})$. The minimum is then $f(\mathbf{x}_0 + \delta_*\hat{\mathbf{n}})$, where $\delta_* = \text{argmin}_\delta g(\delta)$. In the scheme of the previous paragraph, we specialized to $\mathbf{n} = \hat{\mathbf{e}}_i$, and iterated for $i = 1, \dots, p$.

As can be seen in the path from the red point to the blue point in fig. 2.3, scanning along each orthogonal canonical direction can be time-consuming, specially for some functions with long and narrow valleys at some angle with the coordinates basis vectors. The reason why using unit basis vectors can be so inefficient is because optimizing along a given basis vector spoils down the prior minimization carried out in other directions. As a result, the process requires more iterations to crawl to the minimum.

Instead of canonical directions, a more efficient strategy for optimizing consists on constructing a set of special, non-interfering direction vectors for which the minimization
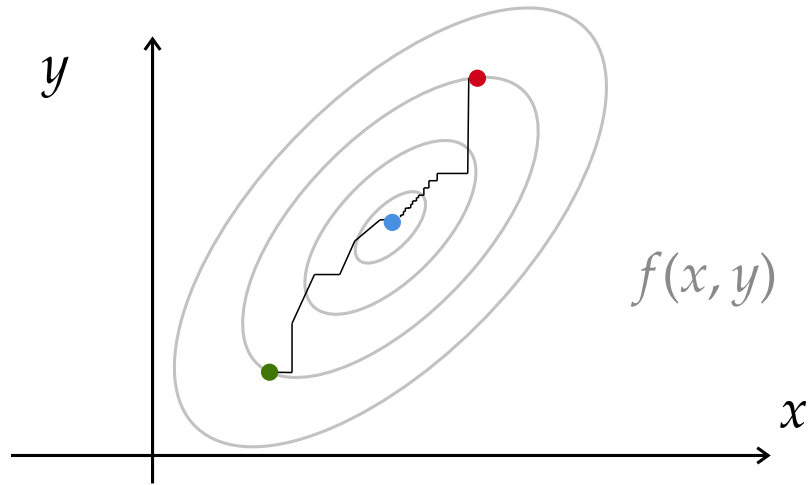
Figure 2.3: Comparison of iterated line-searches until $f(x,y)$'s minimum along canonical unit vectors (path from red dot to blue dot) vs. along vectors chosen according to Powell's method of conjugate directions (path from green to blue dot).

along a direction is preserved when optimizing in a different direction. In ref. [29] the properties that these desired non-interfering vectors should have is discussed. It is shown that the necessary condition for direction vectors $\mathbf{u}$ and $\mathbf{v}$ to be non-interfering is

$$\mathbf{v} \cdot \mathbf{H} \cdot \mathbf{u} = 0, \tag{2.1}$$

where $(\mathbf{H})_{ij} = \partial^2 f(\mathbf{x}_0)/\partial x_i \partial x_j$ is the Hessian matrix for the objective function f. The $\mathbf{u}$ and $\mathbf{v}$ directions are said to be *conjugate* directions.

The question now is on how to find this appropriate set of p conjugate directions. Let $\{\mathbf{u}_i\}$ denote our directions set. Powell [35] proved that conjugate directions can be obtained according to the following algorithm:

1. Let the initial directions be the basis vectors: $\hat{\mathbf{u}}_i = \hat{\mathbf{e}}_i$ for $i = 1, \ldots, p$.

2. Save the starting point (initial parameters state) as $\mathbf{x}_0$;

3. For $i = 1, \ldots, p$ minimize along $\hat{\mathbf{u}}_i$. Save the minimum as $\mathbf{x}_i$.

4. For $i = 1, \ldots p - 1$ set $\hat{\mathbf{u}}_i \leftarrow \hat{\mathbf{u}}_{i+1}$

5. Set $\mathbf{u}_p = \mathbf{x}_p - \mathbf{x}_0$. Normalize to obtain $\hat{\mathbf{u}}_p$.

6. Minimize along $\hat{\mathbf{u}}_p$. Name the found minimum as the new $\mathbf{x}_0$.

7. Repeat the procedure until reaching a certain number of evaluations or until some stopping condition is reached.

In steps 1–3, we optimize along each one of the unit basis vectors, updating the minimum. When finishing optimization along $\mathbf{u}_p$, the current minimum will be $\mathbf{x}_p$. In step 4 we discard the first direction, rename directions $\mathbf{u}_{i+1}$ to $\mathbf{u}_i$, and set as our new p-th direction the vector pointing along the line from the starting point $\mathbf{x}_0$ to the current minimum.

In this loop, steps 1–6 characterize 1 iteration and results in 1 new direction. Powell proved that, for a quadratic form, k iterations of this strategy produces a set of directions whose last k vectors are mutually, pairwise conjugate, in the sense of the Hessian matrix. So p iterations exactly minimizes the quadratic form. The method is also quadratically convergent: each iteration doubles the number of significant figures of the candidate minimum for the quadratic form.

There is a problem, however, in throwing away for $\hat{\mathbf{u}}_1$ for $\mathbf{x}_p - \mathbf{x}_0$ every iteration: at some point the lines start to fold up on each other and lose linear independence. As a result the function can end up minimized only within a subspace of parameter space. To fix this, one can reinitialize the directions to the basis vectors after an iteration along the p directions, or use any new set of orthogonal directions. This means giving up conjugacy and quadratic convergence.

The apparently counter-intuitive solution suggested by Powell is to discard not necessarily $\hat{\mathbf{u}}_1$ in favor of the new direction, but the direction along which f had its largest decrease so far. This is justified because this direction is likely have a large component along the new proposed direction. Powell also posits some conditions in which is best not to add any new directions, keeping the old set from the previous iteration [29, section 10.7]. The resulting algorithm shall is referred to as "Powell's method".

Powell's method results in a set of p directions which are no longer mutually conjugate by the end of p iterations. The search is also no longer quadratically convergent, but it is more adequate for more diverse objective function landscapes. For instance, if the objective function has long, twisting valleys, quadratic convergence guaranteed by conjugate directions is of no use since we may start far away from the nearly parabolic region. In this situation, we would be leaping along the minimum of a parabola which is not quite at the minimum yet. When close to "true" parabolic region, Powell's criteria results in adequate directions which tends to crawl about the paraboloid principal axes quite efficiently.

The path from the green to the blue point in fig. 2.3 illustrates the use of Powell's method for choosing directions. In it, we can see that the two initial search directions were performed along the unit canonical vectors. Next, the direction pointing from the starting point to the minimum after the two first searches is used, and the direction with the largest component along it, $\mathbf{e}_y$, was discarded. Further iterations rendered directions along which the search tends to walk by the principal axis of the paraboloid in a more efficient manner than the searches using unit canonical vectors.

In summary, Powell's method calculates and manages directions adaptively, deciding when to change old directions in favor of the newly calculated vectors, and when to avoid the changes to control build-up of linear dependence. In practice, using Powell's directions accounts to finding a good set of directions providing "shortcuts" towards the minimum in the objective landscape, instead of "zig-zags", as for the case of canonical vectors.

RCDS consists on using Powell's method for managing directions and minimizing along these directions with the noise-robust line-optimizer described previously. RCDS was first implemented by the authors of ref. [15] and is available in Matlab and Python on their GitHub repository. The code used on SIRIUS was based on their implementation. The SIRIUS code is object-oriented and was implemented in Python by members of LNLS' Accelerator Physics Group and the author. The code is available in the "optimization" directory of the Accelerator Physics Suite (apsuite) repository [36]. The pseudocode for the bracketing and line scan routines as well as Powell's directions loop is available in Appendix A.

CHAPTER 3

Storage ring setup, diagnostics, measurements & experimental methods

In this chapter, we delve into the SIRIUS magnetic lattice, beam diagnostics tools and relevant experimental methods. We emphasize the key parameters for optimizing nonlinear dynamics and detail the experimental procedures encompassing beam trajectories and orbits, beam current and lifetime, as well as the control and manipulation of tunes and chromaticity during machine studies. The final segments address the selection of objective functions for probing the Dynamic Aperture and the selection of sextupole families as optimization knobs.

3.1 SIRIUS magnetic lattice

SIRIUS storage ring consists on a 20-cell five-bend-achromat (5BA) lattice comprising a 5-fold symmetric configuration with alternating high and low horizontal betatron functions at the straight sections, as Fig. 3.1 shows. There are 5 A-type sections, with high horizontal betatron function and 15 B- and P-type sections, with low horizontal and vertical betatron functions [37]. A superperiod consists of one high-beta and 3 low-beta sections arranged in the order A-B-P-B.

The central dipole, the BC, is a permanent superbend magnet with a peak field of 3.2 T. The storage ring accommodates 20 such. The arcs contain additional four dipoles: two B1 and two B2. These are electromagnetic dipoles with peak fields of 0.58 T. In total, the SIRIUS magnetic lattice comprises 100 dipoles: 20 permanent BC magnets and 80 B1 and B2s electromagnets.

In the high-beta straight sections, the quadrupole doublet (QFA, QDA) is employed for optics matching. B-type sections utilize the (QDB1, QFB, QDB2) quadrupole triplet for matching while the (QDP1, QFP, QDP2) triplet is used in the P-type sections. The arc sections contain the Q1, Q2, Q3, and Q4 quadrupole families, totalling 12 families of quadrupoles and 270 magnets.

The lattice also features 21 families of sextupoles magnets, used for chromaticity correction and nonlinear dynamics optimization. They sum up to 280 magnets. Some

sextupoles families are located where the dispersion function vanishes and are called *achromatic*, or harmonic, while other families, located where there is non-zero dispersion, are called *chromatic* families.

Table 3.1 lists the sextupoles families and their types in the storage ring. The 21 families are, in principle, the available search space for nonlinear dynamics optimization. The subsection 3.3.2, on the choice of optimization knobs, at the end of this chapter, shows how the search space can be reduced down to 13 dimensions once the constant chromaticity requirement and/or other additional constraints are imposed.
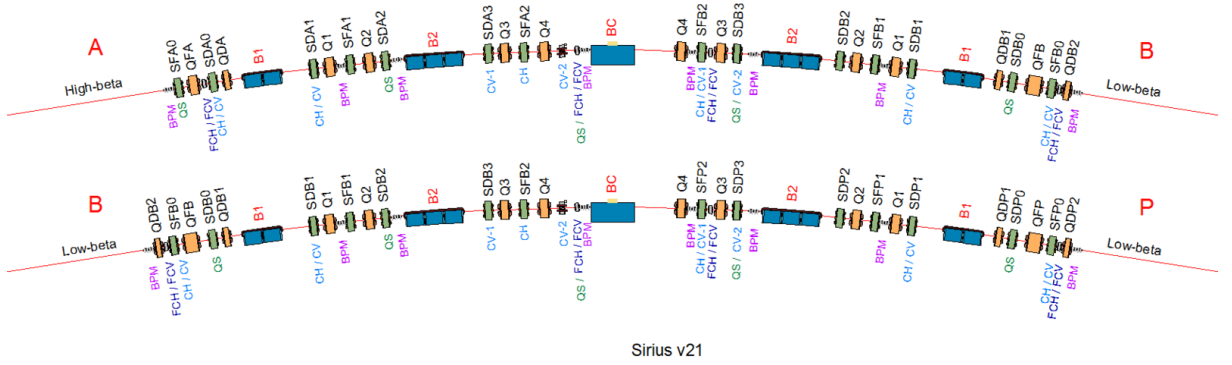
Figure 3.1: SIRIUS 5BA cells comprising the lattice. The cells differ by their straight section types: high-beta type (A), or low-beta (B, P). A superperiod consists of one high-beta and 3 low-beta sections arranged in the order A-B-P-B. The storage ring consists on 5 concatenation of superperiods. Source: Wiki-SIRIUS (currently only available on-campus).

Table 3.1: SIRIUS sextupole families

achromatic	chromatic
SFA0, SDA0, SFB0,	SDA1, SFA1, SDA2, SFA2,SDA3, SDB1, SFB1,
SDB0, SDP0, SFP0	SDB2, SFB2, SDB3, SFP1, SDP1, SDP2, SFP2, SDP3

3.2 Beam diagnostics and measurements

3.2.1 Beam positions

To track the beam's position along the ring, a diagnostic tool known as Beam Position Monitor (BPM) employs a set of four pick-up antennas positioned within the vacuum chamber, as illustrated by Fig 3.2. The mirror charges induced by the electron beam are collected by the antennas. The determination of beam displacements relies on the differential signal induced on the antennas when the beam deviates from the device's geometric and electric center. The induced voltage signal undergoes processing in the "partial-Delta/Sigma" scheme, providing horizontal and vertical beam displacements
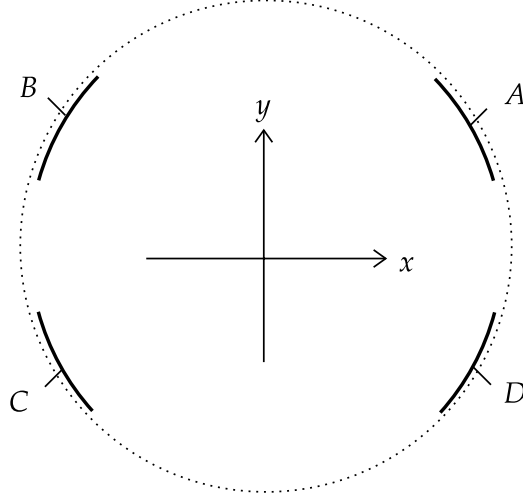
Figure 3.2: Schematic representation of BPM button antennas, in solid lines, the vacuum chamber cross-section, in dashed lines, and the transverse positions reference frame.

through the following algebraic calculations:

$$x = K_x \left[\frac{A - C}{A + C} + \frac{D - B}{D + B} \right], \quad y = K_y \left[\frac{A - C}{A + C} - \frac{D - B}{D + B} \right], \tag{3.1}$$

where A, B, C, and D represent the intensity of the induced signal over the corresponding antennas and K_x and K_y are calibration factors.

SIRIUS is equipped with 160 BPM distributed along the storage ring. The BPMs allow the determination of the centroid's (beam electric center) displacements at a turn-by-turn (TbT) acquisition rate for probing the betatron motion. The signal can also be processed at other acquisition rates, allowing for signal averaging and providing information about the orbit.

Phase-space reconstruction and decoherence

With BPM recording the TbT motion of the beam's centroid, the x and y positions can be readily acquired. The angles, or momenta, can be obtained through the following processing: for two consecutive BPMs located at the ends of a straight section of length ℓ, where no bending or focusing occurs, the beam angle can be calculated as $x' = \frac{\Delta x}{\ell}$, where Δx refers to the difference in the BPMs position readings. This allows for the reconstruction of the x, x' and y, y' phase-spaces on a TbT basis, as exemplified by Fig. 3.3. In the figure, BPM data of the beam was acquired at the TbT rate, soon after betatron oscillations were induced to the beam's centroid. The beam initially had an amplitude in the negative horizontal direction reaching approximately -8 mm and in the first turns it circulated the outermost region of the phase portrait (dark blue points). The last turns correspond to light yellow points in the innermost region.

At first glance, in Fig. 3.3, it might seem that the transverse positions are
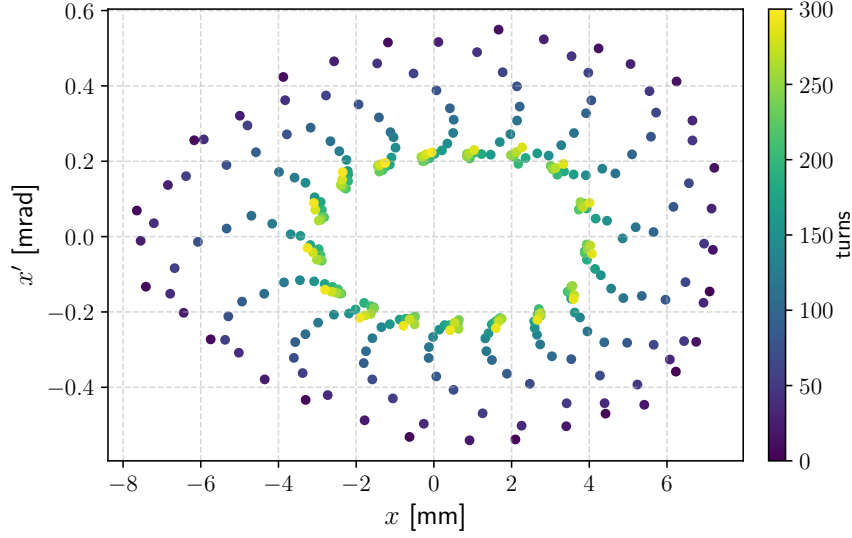
Figure 3.3: Phase space reconstruction from TbT BPM data. Data was collected for 300 turns in the storage ring. The color-scheme encodes the turn each point was collected.

being damped. However, the radiative damping time for the SIRIUS storage ring is of the order of thousands of turns, much more than the acquired time scale in the figure. This apparent damping is a manifestation of *decoherence*. Decoherence arises due to the nonlinear tune-shifts and the finite extent of the beam in 6-dimensional phase space, which has a spread over amplitudes. The cumulative effect of amplitude-dependent and momentum-dependent tune-shifts renders the bunch with a spread in tunes. This results in the filamentation and spreading of an initially localized bunch in phase space due to the different frequencies (the tunes) with which they circulate the ellipses. In this scenario, the positions (and momenta) tend to become uncorrelated, and the average of the electrons distribution, which is the beam's centroid measured by the BPMs, goes to zero, justifying the apparent damping.

3.2.2 Beam current and injection efficiency

Direct-Current Current Transformers (DCCTs) enable the measurement of the stored beam current within accelerator rings (booster or storage ring). The BPMs sum-signal, which is proportional to the beam current, can also be used to measure currents and calculate current variations. In transport lines, there are also Integrated Current Transformers (ICTs) which allow measuring the integrated current (charge) per pulse.

Utilizing the current measurement and the beam revolution period in the respective ring, one can assess the stored charge and calculate the injection efficiency (IE) during storage ring injections. By measuring the charge in the booster or transport line just before injection into the storage ring and the storage ring charge immediately after the injection pulse, it is possible to deduce the efficiency of the injection process.

3.2.3   Tunes measurement & control

When TbT motion is viewed at a fixed longitudinal position s, it consists of the sampling of a harmonic motion, for which the fundamental frequency is the fractional part of the tune ν. Thus, observation of TbT data can reveal the tunes upon the appropriate signal processing. For instance, the betatron motion can be Fourier-transformed (discrete Fourier transform via fast-Fourier transform algorithm), revealing the BPM signal spectrum. Alternatively the time-domain signal can be fitted to a sinusoid, allowing the determination of the tune as the fundamental frequency.

Despite being simple, the process described above is incompatible with user's shift operation, and mostly used during machine experiments for measuring the tunes of large-amplitude motion or for precise determination of changes in tune due to relevant changes in operation parameters. The main incompatibility with user's operation is that extracting tunes from TbT data requires inducing betatron oscillations by kicking and the beam and operating with the BPMs in the TbT acquisition rate. This means the control loops of the Fast Orbit Feedback System (FOFB) and Slow Orbit Feedback System (SOFB), which guarantee the orbit stability required by the beamlines, must be turned-off.

Precise monitoring of the tunes during operation is achieved with the aid of a strip-line shaker, which constantly drives the beam with an alternating electric field in a narrow band of frequencies, leading to sub-nanometer displacements and inducing small-amplitude betatron motion without interfering significantly with the operation. This system also reads back the beam response at that same frequency range. The peak of the beam response signal is identified with the betatron tune.

Regarding changes and manipulation of the tunes, formula (1.25) reveals that adjustments in the quadrupole strengths, particularly at the quadrupoles in large β-function sections, enable control of the tunes. As the tune response to changes in quadrupole strength is linear, a tune-response matrix can be constructed, i.e., the Jacobian of the tunes with respect to changes in quadrupoles, allowing tune changes to be expressed as

$$\Delta\boldsymbol{\nu} = \mathbf{J}_{\nu}\Delta\mathbf{K}, \tag{3.2}$$

where $\Delta\boldsymbol{\nu} = \begin{bmatrix} \Delta\nu_x & \Delta\nu_y \end{bmatrix}^{\mathsf{T}}$ is the tune-shifts vector, $\Delta\mathbf{K}$ is the vector containing the changes in strengths across all the quadrupole families, and the Jacobian or response matrix has entries

$$(\mathbf{J}_{\nu})_{ij} = \frac{\partial\nu_i}{\partial K_j} \approx \frac{\Delta\nu_i}{\Delta K_j}, \quad i = x, y, \quad j \in \text{tune-correction quadrupole families.} \tag{3.3}$$

The system (3.2) can pseudo-inverted, allowing for the determination of quadrupoles

changes required for a desired change in tune

$$\Delta\mathbf{K} = \mathbf{J}_\nu^+ \Delta\boldsymbol{\nu} \tag{3.4}$$

where $\mathbf{J}_\nu^+ = (\mathbf{J}_\nu^\mathsf{T}\mathbf{J}_\nu)^{-1}\mathbf{J}_\nu^\mathsf{T}$ is the Moore-Penrose pseudoinverse. The tune-correction quadrupole families are located in non-dispersive sections

3.2.4 Chromaticity measurements & control

Chromaticity characterizes the energy-dependent tune-shift. To measure it, we need to calculate the numerical derivative

$$\xi_u = \frac{\partial\nu_u}{\partial\delta} \approx \frac{\Delta\nu_u}{\delta}, \quad u = x, y, \tag{3.5}$$

that is, measure the tune-shift $\Delta\nu_u$ induced by the energy-shift δ.

A direct manner to induce a particular energy-shift is to change the RF cavities frequency. A relation can be established between energy deviations δ and relative RF frequency changes with the aid of a quantity α, known as *momentum compaction factor* [11, 21]:

$$\delta = -\frac{1}{\alpha}\frac{\Delta f}{f}. \tag{3.6}$$

Where the momentum compaction factor is defined by

$$\alpha \equiv \frac{1}{L} \oint G(s)\eta(s)\,\mathrm{d}s, \tag{3.7}$$

and is first introduced to relate changes in orbit length due to energy deviations [11].

Therefore, in practice, when measuring chromaticity, we are interested in the following numerical derivative, which is a consequence of eqs. (3.5) and (3.6):

$$\xi_u = -\frac{f}{\alpha}\frac{\Delta\nu_u}{\Delta f}. \tag{3.8}$$

The derivative is usually calculated by obtaining the first-degree coefficient of the polynomial fitting of the tune-shifts vs. RF frequency curve.

Regarding chromaticity control, eq. (1.33) shows that chromaticity depends linearly on the strengths of the chromatic sextupole families. Thus it can be adjusted to certain desired values according to the same pseudo-inversion procedure described above for the tunes. We relate the changes in chromaticity $\Delta\boldsymbol{\xi}$ to the changes in the strengths of the sextupole families $\Delta\mathbf{S}$ by

$$\Delta\boldsymbol{\xi} = \mathbf{J}_\xi \Delta\mathbf{S}, \tag{3.9}$$

where $\Delta\boldsymbol{\xi} = \begin{bmatrix} \Delta\xi_x & \Delta\xi_y \end{bmatrix}^\mathsf{T}$ and the Jacobian matrix $\mathbf{J} \in$ has entries

$$(\mathbf{J_\xi})_{ij} = \frac{\partial\xi_i}{\partial S_j} \approx \frac{\Delta\xi_i}{\Delta S_j}, \quad i = x, y, \quad j \in \text{chromaticity correction sextupole families.} \quad (3.10)$$

If we wish to change chromaticity by a $\Delta\boldsymbol{\xi}$ amount, the Jacobian can be pseudo-inverted to calculate the required sextupole strength changes:

$$\Delta\mathbf{S} = \mathbf{J}_\xi^+ \Delta\boldsymbol{\xi}. \quad (3.11)$$

In practice, the chromaticity Jacobian was never measured in the actual machine, due to the time-consuming process of varying each sextupole family individually and carrying out the chromaticity measurement. The "measurement" of the Jacobian is instead carried out in the SIRIUS storage ring computer model. The model-calculated Jacobian renders satisfactory chromaticity corrections in the actual machine.

3.3 The choice of objective function & optimization knobs

3.3.1 The objective function

There is no analytical formula relating the storage ring linear or nonlinear optics to the Dynamic Aperture (DA). The optimization procedure must be a heuristic search procedure: changes are performed to the knobs (nonlinear magnets) and the effect on the DA is evaluated. Additionally, one cannot measure the DA in a practical and straightforward measurement procedure sufficiently fast to be run online. Direct measurements of DA can take several iterations of acquiring trajectories of the beam with increasingly higher transverse displacements. The acquisitions are then processed to access the DA.

For online optimization one must choose a practical, relatively fast to measure objective function to act as a probe of the DA: a figure of merit related to the DA to represent it and to be used to evaluate the quality of the changes performed during the online tuning process. In our experiments, we studied using two practical objectives as the probes for DA: the **injection efficiency** (IE) and the **beam's resilience to dipolar perturbations**. The former is quite self-explanatory: the larger the DA, larger the space for the beam to be captured into the storage ring during the injection pulse, and thus the larger the injection efficiency.

Figure 3.4 illustrates how a smaller aperture, shown in red, influences the efficiency of injection. After leaving the booster accelerator at 3 GeV, the beam is transported into the storage ring injection straight section. It reaches the injection area
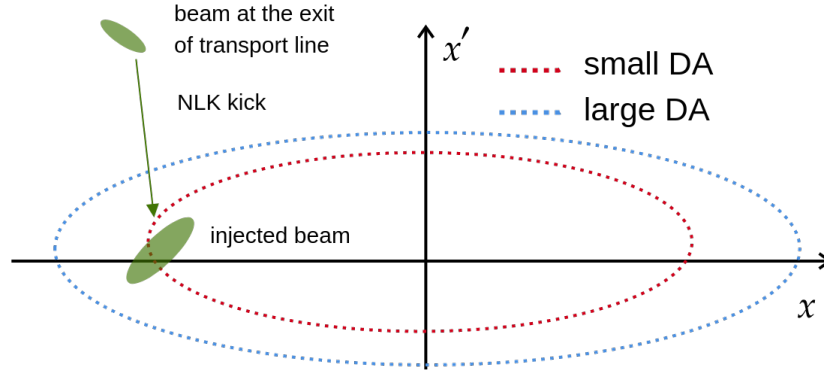
Figure 3.4: Illustration of injection sensitivity to the DA. In red, the DA border before optimizing sextupoles. In blue, the expected effect on the DA border after optimization. Reduced injection efficiency results from losing part of the beam due to small DA. Optimizing injection efficiency by tuning sextupoles should translate to optimizing DA.

with phase space coordinates of approximately $(x, x') \approx (-8 \text{ mm}, 3 \text{ mrad})$. The beam then suffers the deflection of a nonlinear pulsed magnet, the nonlinear kicker (NLK) and is captured into the storage ring with phase space coordinates $(-8 \text{ mm}, 0)$ [12]. If the DA border along the negative horizontal direction is reduced below -8 mm, the dynamics may not accommodate the long term time evolution of the beam fraction exceeding this threshold. This fraction is lost due to the nonlinear dynamics instabilities in the first turns. On the other hand, if the DA is increased, the larger the beam fraction which is successfully captured and survives in the storage ring in the long term.

As for the beam kick resilience, this figure of merit is related to the DA by the following reasoning: the larger the horizontal dipolar kicks the beam can survive, the larger the orbit distortions towards the positive or negative horizontal direction (depending on the kick direction). So the larger the amplitudes the beam explores as it oscillates. If the beam survives to larger kicks, it means the ring can accommodate larger orbit distortions because of an increased DA.

Figure 3.5 illustrates the phase space orbits for a beam when it is kicked. In the left sketch, small amplitude TbT motion ellipse is shown. When kicked, the beam gains momentum (angle) and is rigidly translated higher along the x' direction. In the linear approximation the beam goes from one ellipse, with action J to another ellipse, with action $\tilde{J} > J$. If the kick is stronger (larger than 500 μrad), the action jump takes the beam to a nonlinear regime, as shown in the right sketch, where the beam traces out distorted ellipses. After the kick, the maximum amplitude reached in the negative horizontal direction is increased thus the larger the fraction of the beam that can survive the kick, the larger the DA.

In summary, the dynamic aperture optimization procedure must consist on the exploration of sextupole (knobs) configurations yielding the largest dynamic aperture as accessed by as objective function such as injection efficiency or beam kick-resiliency.
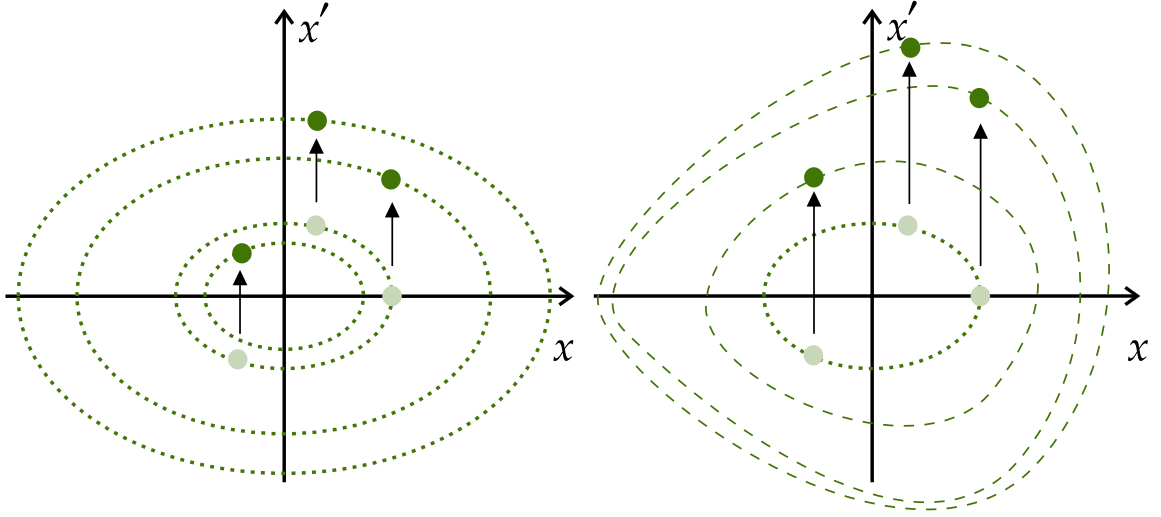
Figure 3.5: Action jumps due to dipolar kicks in the linear (left) and nonlinear (right) regimes.

3.3.2   The optimization knobs

The DA is determined by the quality of the beam dynamics in terms of perturbations. Given that a linear optics correction scheme is already in place and regularly implemented in the machine, effectively addressing optics functions and phase advances, the primary factor impacting SIRIUS DA likely stems from nonlinear dynamics and/or remaining uncorrected and previously inaccessible deviations and errors. This may include sextupole field errors or other minor nonlinear multipoles.

If the limitation of the DA is likely associated with nonlinear dynamics, the actuation knobs must unexpectedly be composed of the controllable nonlinear magnets available at the SIRIUS storage ring, namely the sextupoles. However, it is important to note that sextupole strengths cannot be changed arbitrarily.

Sextupoles are originally introduced into the lattices as actuators for correcting chromaticity, which refers to the energy-dependent aberrations in the focusing of the beam, and optimizing DA. Care must be taken when varying the sextupole strengths, as it can alter the chromaticity.

A strategy needs to be devised to select the sextupole family in a way that allows for the simultaneous correction of chromaticity and the online tuning of magnet strengths to optimize the DA. In simpler terms, the optimization processes for DA should be conducted while preserving the machine's chromaticity. The natural question that arises is how to implement these isochromatic changes to the sextupoles.

As highlighted previously, SIRIUS has 21 sextupole families, magnets powered by the same power supply. Six of them are achromatic families, strategically placed where the dispersion is zero, while the remaining 15 families are chromatic families. In principle, the optimization parameter space is 21-dimensional. However, as mentioned earlier, the goal is to change sextupoles without affecting chromaticity. Since we need at least one

degree of freedom for correcting chromaticity in the horizontal plane and one degree of freedom for correcting chromaticity in the vertical plane, there are 19 independent knobs available. The dimensionality of the search space can be further reduced by imposing additional constraints on certain families' variations. These specific constraints changed according to each experiment and are detailed in what follows. Two strategies were adopted to select the sextupole optimization knobs: a compensation scheme and using the Jacobian null space knobs.

Compensation scheme

The idea is the following: out of the 15 chromatic sextupole families, at least two of them are labeled "correction" or "compensation" families and are not freely varied by the optimization routine during the experiment. The other 13 chromatic families can be varied arbitrarily, respecting their linear magnetic (non-saturated) regime. Alongside these 13 chromatic families, the strength of the 6 achromatic sextupole families are also free knobs. Whenever the routine proposes changes in the free knobs, the chromaticity changes caused by this action are anticipated as follows: the reduced Jacobian, $\tilde{\mathbf{J}}_\xi$, whose columns contain only those corresponding to the free knobs, is used to calculate the chromaticity change $\Delta\boldsymbol{\xi} = \tilde{\mathbf{J}}_\xi \Delta\mathbf{S}_{\text{free}}$ upon the change $\Delta\mathbf{S}_{\text{free}}$ in the free knobs. Another reduced Jacobian, $\mathbf{J}'_\xi$ containing only the columns corresponding to the "correction" or "compensation" families is used to counteract the predicted chromaticity build-up, i.e., to produce sextupole changes $\Delta\mathbf{S}_{\text{corr.}}$ leading to exactly the opposite chromaticity change $-\Delta\boldsymbol{\xi}$. The required strength changes in the compensation families is determined by $\Delta\mathbf{S}_{\text{corr.}} = \mathbf{J}'^{+}_\xi(-\Delta\boldsymbol{\xi})$. Applying $\Delta\mathbf{S} = \Delta\mathbf{S}_{\text{free.}} + \Delta\mathbf{S}_{\text{corr.}}$ to the machine leads to sextupole families strength changes keeping the chromaticity unchanged. The scheme is illustrated in Fig. 3.6.

In practice, during the experiments, the compensation scheme was used as follows. The 6 achromatic families plus the SDA1, SFA1, SDB1, SDP1, SDA3, SDB3 and SDP3 families could be freely varied. Their strengths were the optimization knobs. The SDA2, SDB2, SDP2, SFA2, SFB2 and SFP2 were used as the compensation or correction families. They would only be varied to cancel the chromaticity build-up caused by changing the free knobs. The resulting search space was 13-dimensional.

Note that families SFP1 and SFB1 were not used as knobs. They were kept constant. They were actually used in the first experiments attempts, as discussed in section 4.1 of the next chapter, but were later removed upon the realization that they already operate close to saturation, where the fields may not be repeatable due to hysteresis effect. When these are included, the search space is 15-dimensional.

The compensation families were chosen on basis of having range to act on the chromaticity, that is, they were the families with initial strengths far from saturation, with a lot of room to compensate the knobs effects on chromaticity.
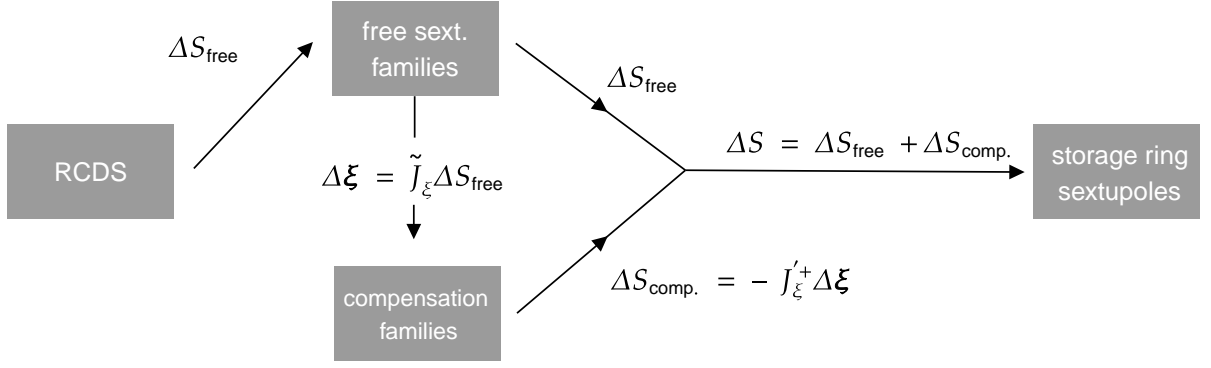
Figure 3.6: Illustration of the compensation scheme for changing sextupole strengths with no change in chromaticity.

Jacobian null space knobs scheme

Here the idea is to identify the combination of sextupole families living in the null space, or kernel, of the chromaticity Jacobian matrix. That is, we are interested in the set of vectors $\ker(\mathbf{J}_\xi) = \mathrm{span}\{\mathbf{s}_i \in \mathbb{R}^{21} | \mathbf{J}_\xi \mathbf{s}_i = \mathbf{0}\}_{i=1,\dots,19}$. If we perform changes along such subspace $\Delta\mathbf{S} \in \ker(\mathbf{J}_\xi)$ then the resulting changes in chromaticity are null.

The reason why we can anticipate the dimension of the null space is 19 is because it contains the 6 achromatic sextupole families plus 13 degrees of freedom out of the 15 achromatic families, since at least 2 degrees of freedom are needed to act over chromaticity.

A straightforward way to identify the null space of the Jacobian is to calculate its full singular value decomposition (SVD), which expresses the Jacobian as the product

$$\mathbf{J}_\xi = \mathbf{U}\mathbf{\Sigma}\mathbf{V}^\mathsf{T}$$

$$= \underbrace{\begin{bmatrix} \vdots & \vdots \\ \mathbf{u}_1 & \mathbf{u}_2 \\ \vdots & \vdots \end{bmatrix}}_{2\times 2} \underbrace{\begin{bmatrix} \sigma_1 & 0 & \dots & 0 \\ 0 & \sigma_2 & \dots & 0 \end{bmatrix}}_{2\times 21} \underbrace{\begin{bmatrix} \dots & \mathbf{v}_1^\mathsf{T} & \dots \\ \dots & \mathbf{v}_2^\mathsf{T} & \dots \\ \dots & \mathbf{v}_3^\mathsf{T} & \dots \\ & \vdots & \\ \dots & \mathbf{v}_{21}^\mathsf{T} & \dots \end{bmatrix}}_{21\times 21}. \tag{3.12}$$

Note that the singular-values matrix has only two non-vanishing singular values σ_1 and σ_2. In the sum-over-modes form of SVD, we have

$$\mathbf{J}_\xi = \sum_{i=0}^{21} \sigma_i \mathbf{u}_i \mathbf{v}_i^\mathsf{T} = \sigma_1 \mathbf{u}_1 \mathbf{v}_1^\mathsf{T} + \sigma_2 \mathbf{u}_2 \mathbf{v}_2^\mathsf{T}, \tag{3.13}$$

in which it becomes clear that we have only two independent modes or degrees of freedom for changing chromaticity, corresponding to the horizontal and vertical degrees of freedom.

Multiplication of the SVD-decomposed $\mathbf{J}_\xi$ by $\mathbf{V}$ gives $\mathbf{J}_\xi \mathbf{V} = \mathbf{U}\mathbf{\Sigma}$, which
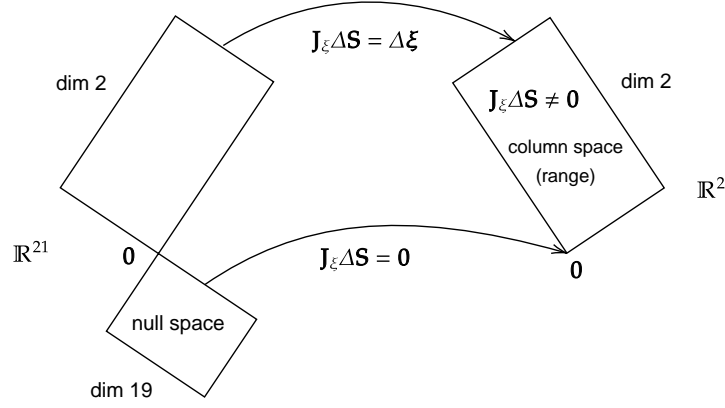
Figure 3.7: Illustration of chromaticity jacobian $\mathbf{J}_\xi$ fundamental subspaces. The idea is to use sextupole combinations living in the null space, since these are mapped to the zero vector on the chromaticity space.

explicitly reads

$$\mathbf{J}_\xi \mathbf{v}_i = \sigma_i \mathbf{u}_i, \quad i = 1, 2,$$
$$\mathbf{J}_\xi \mathbf{v}_i = \mathbf{0}, \quad i = 3, \ldots, 21. \tag{3.14}$$

Revealing the sextupole strength vectors living in the null space of the Jacobian. They must be the ones associated with the vanishing singular values: $\ker(\mathbf{J}_\xi) = \mathrm{span}\{\mathbf{v}_i\}_{i=3,\ldots,21}$. Figure 3.7 illustrates the fundamental subspaces associated with the chromaticity jacobian. The range of the matrix, or column space, is the chromaticity changes space. Vectors living in the null space are the sextupole strengths combinations mapped to the chromaticity space origin.

As mentioned previously, additional constraints on the families strengths variations have been imposed to further reduce the dimensionality of the search space. In such cases, the jacobian is recalculated considering the imposed constraints. For instance, in one of the experiments the following constraints were imposed:

- Families SFP1 and SFB1 were kept constant, i.e., were not allowed to change. As mentioned, they operate close to their saturation, nonlinear regime, and one cannot trust they would be able to provide reproducible magnetic field changes. Deciding not using them already reduces from 21 to 19 degrees of freedom.

- The pair of families SDB1 & SDP1, SDB2 & SDP2, SFB2 & SFP2, SDB3 & SDP3 were constrained to change by the same amount, starting from their respective initial strengths. This reduces the available options from 19 to 15 families.

These 15 families consist on the combination of the 6 achromatic families, the 4 pairs of constrained families and 5 other non-constrained families SDA1, SFA1, SDA2 , SFA2, and SDA3. Calculating the null space of the Jacobian results in a 13-dimensional search space. We shall refer to such constraint configuration as **Constraint Scheme I**, to distinguish it from **Constraint Scheme II**, which consists on

- Families SFP1 and SFB1 were kept constant, by the same reason as in the previous scheme.

- No pair-wise constraints were imposed to the sextupole families. So, in principle, there were 19 possible families: 21 minus the two families not used.

Calculating the Jacobian null space revealed the 17 chromaticity-preserving free knobs.

CHAPTER 4

Experiments with Online Optimization of Nonlinear Dynamics

This chapter presents the results of the experiments carried out during the this masters project. There are two set of important results: i) those of the experiments carried out in late 2022 and ii) those of the experiments carried out during the first semester of 2023. In i), the early attempts, the experimental method and setup was still being perfected. We tried using the beam kick resilience as objective function and learned it was not the best choice. In ii), we moved on to using instead the injection efficiency (IE) as objective, which had a better performance. We started to be more cautious when choosing the knobs, avoiding the families close to their magnetic nonlinear regime and experimenting with different possibilities of constraints among the sextupole families. We also carried out optimization in different working tunes and performed characterizations and analysis of the configurations found by optimization.

4.1 Kick resilience optimization attempt

In the first attempt to online optimize the nonlinear dynamics, we used the beam kick resilience as objective function. As described in subsection 3.3.1, we sought to minimize the beam-loss rate at a given fixed dipolar kick from the pinger magnet. The idea was to minimize the rate for a given kick, increase the kick and repeat the process, reaching higher survival rates at stronger kicks.

4.1.1 The knobs

The knobs were chosen according to the compensation scheme described in subsection 3.3.2: the achromatic families SDA0, SDB0, SDP0, SFA0, SFB0, SFP0, and the chromatic families SDA1, SDB1, SDP1, SDA3, SDB3, SDP3, SFA1, SFB1, SFP1 varied freely. The SDA2, SDB2, SDP2 and SFA2, SFB2, SFP2 families were the compensation families used to keep chromaticity constant when varying the optimization knobs. In this early attempt, families SFP1 and SFB1 were included as knobs. In later attempts

they were avoided upon the realization that they operate close to the magnets' nonlinear response regime. The search space was 15-dimensional.

4.1.2   Objective function and setup

A small beam current was accumulated into the storage ring, usually 10 mA, localized in a single bunch. At a given moment, we can fire up the kick from a dipole kicker, located close to the injection section. The BPMs acquisition was fired in synchrony with the kick. Since we are interested in optimizing the horizontal DA, the kick was in the horizontal direction.

To evaluate the beam loss we used the BPMs sum-signal, which is proportional to the stored current. The average sum-signal of the first 10 turns was compared to that of the last 10 turns of the BPMs acquisition time-series. The kick strength was chosen to render an initial beam rate loss of about 35% up to 60%

4.1.3   Optimization runs & results

With the compensation scheme for changing strengths in the sextupole families, RCDS was launched to minimize the beam-loss resulting from the horizontal kick. In the algorithm's first iteration , beam loss dropped from 60% to nearly 0%. In the beginning of the 2nd iteration, the objective function took negative values, which is a numerical artifact, so the optimization run was stopped. The beam-loss minimization significantly improved the beam's resiliency to dipole kicks. After the optimization, it was necessary to kick the beam with a strength of approximately $\Delta x' = -0.850$ mrad to achieve the same 30–60% beam-loss rate previously achieved by a $\Delta x' = -0.760$ mrad kick.

By the end of this first attempt, the machine magnets were standardized[1] and the configurations found during optimization were loaded into the machine sextupoles. This was done to test the repeatability of the configuration found.

Given the improvements in the resilience, it was expected the IE would also improve as a result of the DA enlargement, however, when trying to inject for beam accumulation, the efficiency was quite low, indicating no DA improvements in the $-x$ direction.

The improved kick resilience, however, was preserved. This observation raised the suspicion that the aperture along the negative horizontal direction might have been negatively impacted by the procedure, while the aperture along x' increased. In other words, the DA enlargement was not evenly distributed along both x and x'. The DA border apparently is way more elastic than anticipated, and apparently can be stretched

---

[1]Standardizing magnets consists of driving their power suplies with different types of waveforms to mitigate hysteresis effects and bring the magnets yokes to their standard reference magnetization.

preferentially along x or x', as the Figure 4.1 illustrates. This observation motivated the adoption of IE to probe the DA.
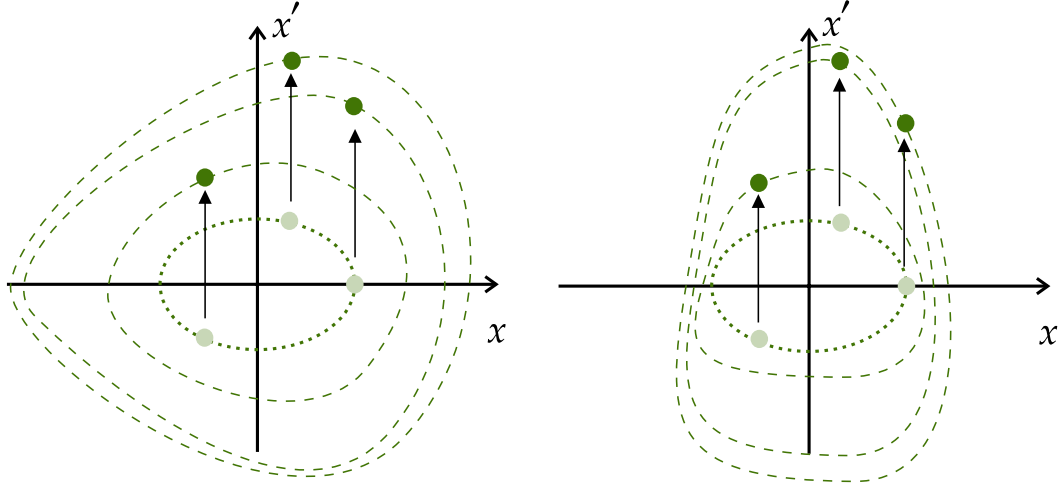

Figure 4.1: Expected phase space ellipse distortions, in the left. Hypothetically realized distortions, preferentially along the x' axis, in the right.

4.2   Injection efficiency optimization

The initial attempt to optimize the DA by minimizing beam loss revealed that the optimization procedure did not enhance IE, suggesting there was no effect over the DA in the x direction. This led to the decision to use the IE itself as the objective function.

In this setup, changes are made to the sextupoles, and each evaluation of the objective function involves taking the average of efficiency of 5 injection pulses into the storage ring. With this configuration, the expected error of the objective function was approximately $\sigma = 1\%$.

The ideia behind optimizing IE is to change the injection conditions to deliberately reduce the efficiency by delivering the incoming beam right on the DA border. The subsequent improvement in efficiency would be a result of DA enlargement. Extra attention was given to the injection conditions and the anticipated beam positions in phase space during this process, taking into account the seemingly elastic nature of the DA boundary. The IE was intentionally reduced by lowering the NLK kick strength, which results in placing the beam slightly above the nominal value of $x' \approx 0$. In practice, a value of $x' \approx 0.100$ mrad was typically set in the experiments. Consequently, the beam was injected at the upper-left border of the (x, x') aperture, as illustrated in Fig. 4.2. The efficiency under such conditions was approximately 30%.

The expectation was that maximizing IE in these conditions would correspond to a more even enlargement of the DA in both the x and x' directions, stretching the boundary diagonally in the upper-left quadrant. This is in contrast to the previous attempt,
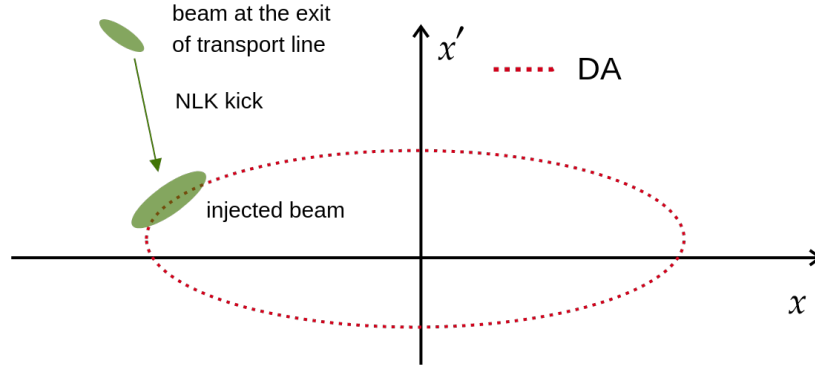
Figure 4.2: Injection conditions for DA optimization.

where the enlargement seemed to occur preferentially along the x' direction. Once the procedure is complete, the DA is anticipated to be larger than in the initial state, and it is expected that injection under nominal conditions $(x, x') \approx (-8 \text{ mm}, 0)$ would be significantly more efficient.

A significant difference from the early attempt was the exclusion of families SFP1 and SFB1 as knobs in the optimization experiments. This decision was made upon realizing that these families operate near their saturation strengths, where hysteresis effects become prominent, as discussed in Section 3.3.2.

The optimization experiments were conducted in the machine with the implemented tunes $(\nu_x, \nu_y) = (49.08, 14.14)$, referred to as WP1, as well as in the tunes $(49.20, 14.25)$ and $(49.16, 14.22)$, denoted as WP2 and WP3, respectively. As mentioned earlier, the goal was to explore a different optics configuration with smaller orbit amplification factors to enhance orbit stability. Part of the results reported below have been presented in ref. [20].

4.2.1 Optimization in Working Point 1 (49.08, 14.14)

The knob selection scheme followed the 13-dimensional search space of Constraint Scheme I, as detailed in Section 3.3.2. Three optimization experiments were conducted, resulting in three optimized configurations.

In Run 1, the optimization began with the reference sextupole configurations loaded in the machine. The machine underwent linear optics and orbit corrections before initiating each run's optimization process. Optimization was launched and once the best IE was achieved and no indication of further improvement was at sight, the run was halted and the best-performing sextupole configuration was saved. These optimal configurations are referred to as "solutions".

The magnets were standardized, and the solution from Run 1 was implemented in the machine. Run 2 commenced with the solution from Run 1. Since the Run 1 solution improved the efficiency, the beam's horizontal offset during injection was further increased
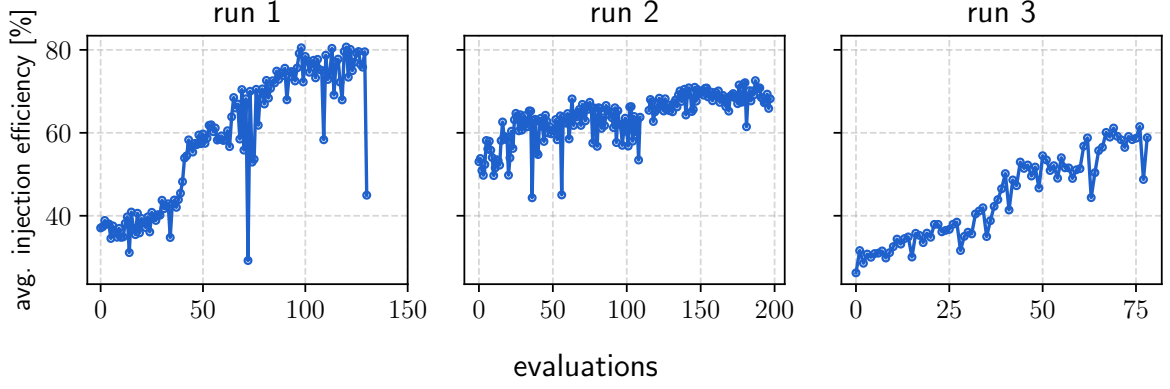
Figure 4.3: Objective function history during the RCDS runs in WP1.
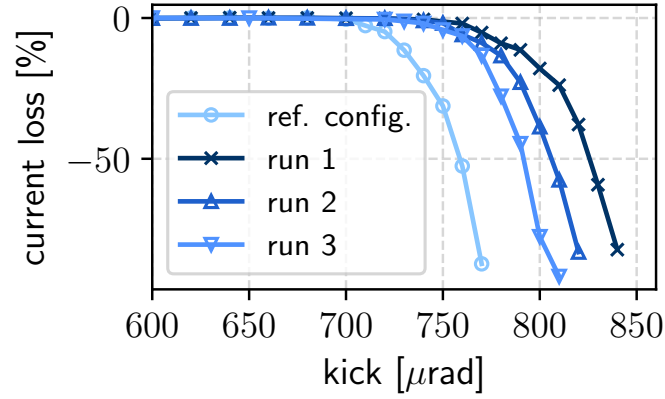
Figure 4.4: Current losses vs. horizontal dipole kick for the ref. config. and for the RCDS solutions at WP1.

in the negative direction to reduce the efficiency by shifting the beam toward the border of the expectedly enlarged DA. The same procedure was replicated for Run 3, which initiated from the solution obtained in Run 2. Figure 4.3 shows the history of the objective function (average efficiency of 5 injection pulses) throughout the optimization runs at Working Point 1.

Characterization of solutions

For each of the optimal configurations identified in Runs 1, 2, and 3, as well as for the non-optimized reference configuration (ref. config.), turn-by-turn (TbT) BPM data of the stored beam subjected to horizontal kicks from the dipolar kicker was collected. The DCCT current monitor allowed the determination of the current losses as a function of the horizontal kicks strengths, which is shown in Fig. 4.4 for the three runs. These curves characterize the beam's resilience to kicks.

TbT data also allowed for the reconstruction of the (x, x') phase space of the beam under the influence of the kicks. Using two BPMs at the ends of an empty ID straight section, the position and angle of the beam were determined at each turn. Figure 4.5 shows

Figure 4.5: Measured phase space at SA05 high-beta straight section for the ref. config. and the best RCDS configurations of runs 1, 2 and 3 in WP1. Color-map indicates the turns. The areas are in mm mrad. The beam was being kicked horizontally at 730 µrad in the ref. config, 790 µrad in run 1, 780 µrad in run 2, and 770 µrad, in run 3. Loss rates of 12%, 11%, 13% and 13%.

the measured phase spaces for the ref. config. and the best configurations found during run 1, 2, and 3, at the storage ring fifth straight section (SA05), which is 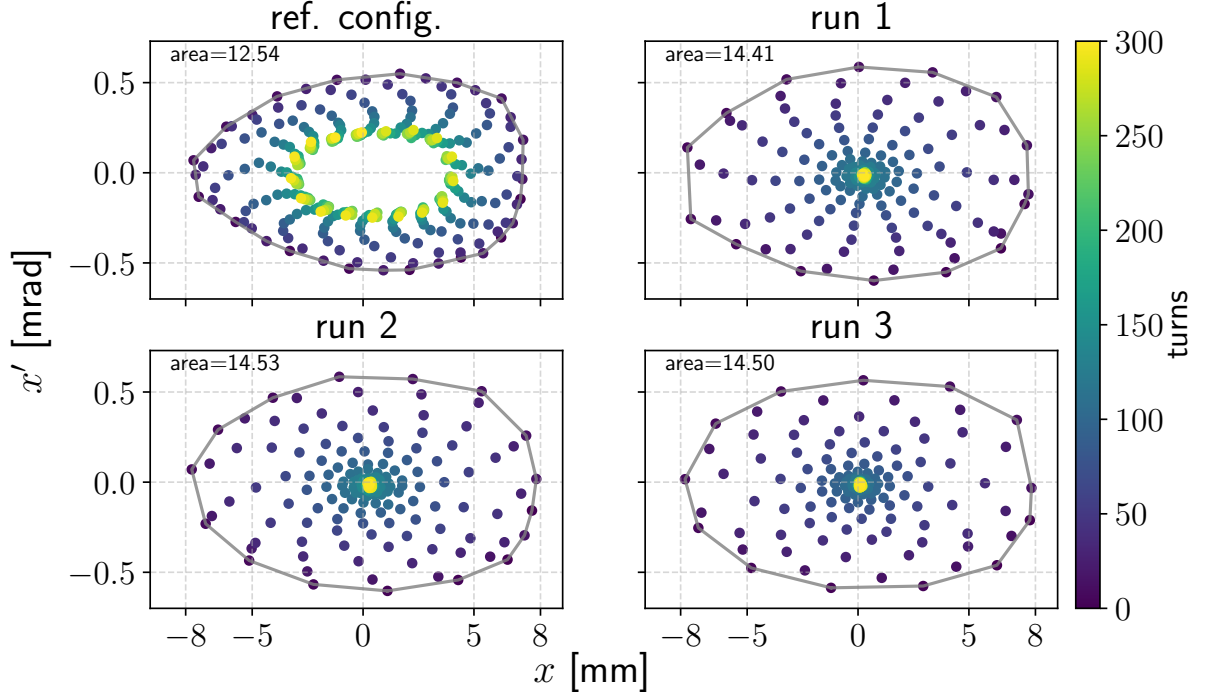a high-beta section with optics identical to that of the injection point. In the measurement, the beam was under the influence of kicks rendering approximately tehe same current loss of 12%.

Table 4.1 compiles the injection efficiencies achieved for each configuration during off-axis NLK injection under normal injection conditions ($x \approx -8$ mm, $x' \approx 0$), as well as the lifetime at 60 mA current for the ref. config. and runs 2.

Once again, we emphasize the apparent elasticity of the phase portrait ellipse deformations: the configuration with the highest kick resilience, observed in Run 1, is not necessarily the one with the largest phase space area and best IE performance. This behavior could be explained if the phase space deformations of the ellipse at the kicker location for this sextupole setting resulted in a larger x'/x ratio, contributing to a greater kick acceptance and poorer injection performance compared to Run 2. In summary, increased kick resilience does not necessarily translate into an increased DA.

Lifetime at 60 mA was measured at 20 hr for run 2 solution, the best performing in terms of IE. The measurement revealed no impact of the optimization procedure on lifetime, since lifetime for the same conditions on the reference configuration is 21 hr.

Despite the precautions taken to avoid changing chromaticity during the optimization procedure by selecting the chromaticity Jacobian null space knobs, slight changes

were observed. Chromaticity was measured as $(2.33, 2.53)$ in the reference configuration and $(2.24, 2.39)$ in the solution obtained in Run 2. This could be attributed to minor discrepancies between the machine computer model and the actual machine, since the optimization knobs were computed using the storage ring computer model Jacobian. Despite the small deviations in chromaticity, the observed values still fall within acceptable operation ranges for the SIRIUS storage ring, according to the transverse instabilities studies shown in chapter 7, section 3 of ref. [25].

In summary, for WP1: the solution found during run 2 rendered 98% IE; increase in horizontal phase space area and horizontal kick resilience were observed; no significant effect was observed on beam lifetime; small, acceptable chromaticity changes observedIncrease in efficiency, phase space areas and kick resilience are strong indicators of a DA enlargement. The online optimization was extremely succesful on WP1.

Table 4.1: Injection efficiency in nominal off-axis conditions & lifetime for optimized configurations at WP1, with tunes $(49.08, 14.14)$.

configuration	injection efficiency [%]	lifetime @ 60 mA
ref-config	88 ± 8	21 hrs
run 1	91 ± 1	
run 2	98 ± 1	20 hrs
run 3	87 ± 3	

4.2.2 Optimization in Working Point 2 (49.20, 14.25)

The storage ring tunes were adjusted to $(\nu_x, \nu_y) = (49.20, 14.25)$. The initial sextupole configuration was the same as the nominal tunes reference configuration. The new working point significantly impacted on the DA, since the IE in nominal conditions with this setup was about 50%, at most. Without successful optimization, it would be impossible to operate in this working point.

For the optimization experiment, the objective function was the IE with the the beam delivered at the upper-left border of the x, x' phase space, just as in the WP1 experiment. The optimization knobs were those of the Constraints Scheme II, discussed in 3.3.2, totalling 17 independent knobs.

Two optimization runs were carried out: run 1 and run 2. The sextupoles were optimized in the new tunes starting with reference sextupoles. Once the best solution from run 1 was identified, it was re-loaded in the machine and, starting from it, run 2 was launched. The objective function history throughout the optimization is shown in Fig. 4.6. Several drops in efficiency can be observed in a single run. This is because, in this experiment, there were "sub-runs": whenever the objective function improvement was slow, the optimization was paused and the IE was worsened by increasing the beam's offset in the horizontal direction during injection. This was a manner to introduce more variability

to see if it could help in accelerating the rate at which the objective was maximized.
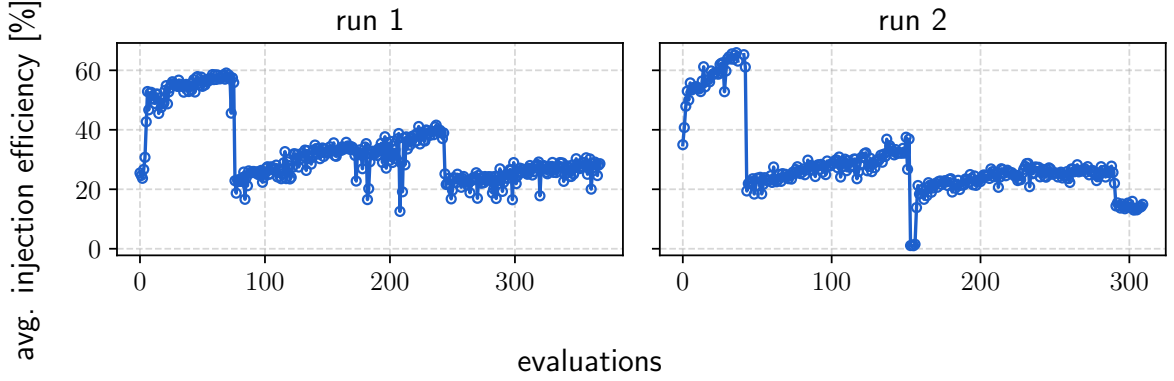
Figure 4.6: Objective function history during the RCDS runs in WP2.

Characterization of solutions

TbT BPM data of the kicked stored beam in the initial configuration (non-optimized) and in each run's best solution was acquired and allowed the determination of current losses vs. kicks, shown in Fig. 4.7, and the reconstruction of phase space, shown in Fig. 4.8. Improvements on the resilience and the phase space area can be observed in the optimized solutions.

Table 4.2 compiles the IEs in nominal injection conditions for each run, as well as the beam lifetime for the non-optimized configuration and run 1 configuration. Run 1 configuration rendered the best IE, the largest kick resilience. It also displayed larger lifetime than the initial configuration, reaching a value comparable to the reference configuration lifetime at WP1. The largest phase space area increase was also observed for this solution. Still, the IE it delivered was quite unsatisfactory and the overall impression was that optimizing in this working point was quite difficult, as the objective function
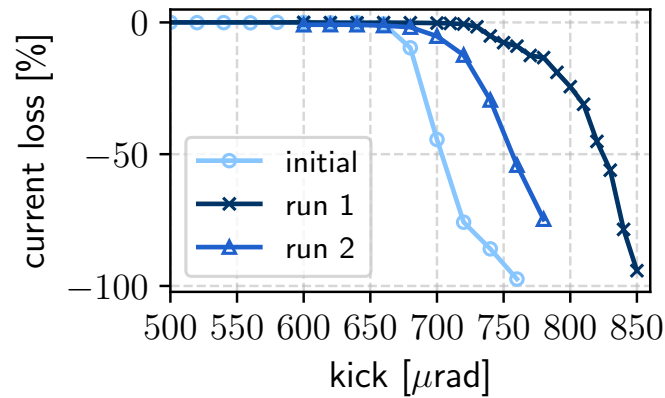
Figure 4.7: Current losses vs. horizontal dipole kick for the initial configuration and the RCDS solutions at WP2.
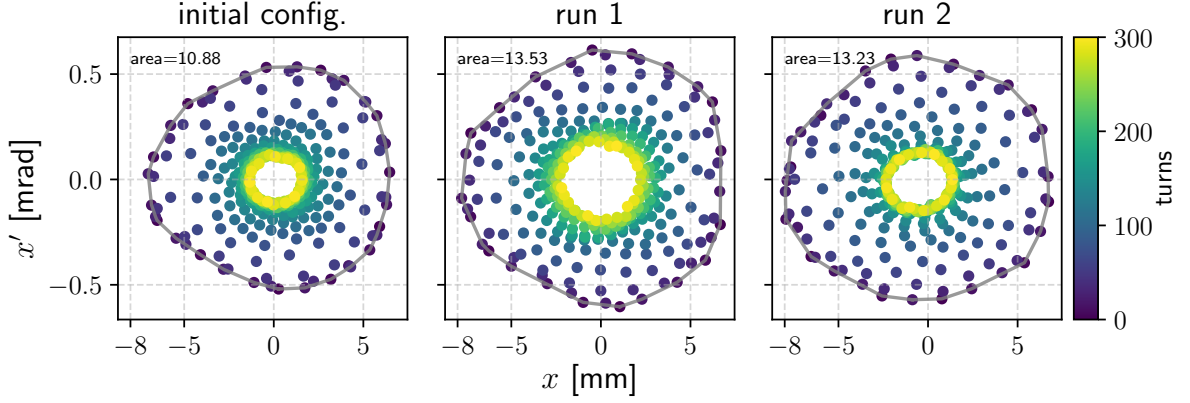
Figure 4.8: Measured phase space at SA05 high-beta straight section for the initial configuration and the best RCDS configurations of runs 1 and 2 in WP2. Color-map indicates the turns. The areas are in mm mrad. The beam was being kicked horizontally at 680 µrad, for the initial configuration, 770 µrad for run 1, and at 720 µrad for run 2. Loss rates of 10%, 12% and 12%, respectively

history of Fig. 4.6 shows. The objective rise was slow and seemed to have the 35% mark as upper limit when the injection was deliberately worsened during the runs. In other words, the DA seemed more rigid. For this reason, another working point was sought. If the idea is to increase the fraction parts of the tunes, and $(0.20, 0.25)$ seemed like overshooting towards unknown regions, optimization in the intermediate tunes between WP1 and WP2, with fractional tunes $(0.16, 0.22)$, seemed reasonable.

Table 4.2: Injection efficiency in nominal off-axis conditions & lifetime for optimized configurations at WP2, with tunes $(49.20, 14.25)$.

configuration	injection efficiency [%]	lifetime @ 60 mA
non-optimized	51 ± 1	18 hrs
run 1	79 ± 3	21 hrs
run 2	65 ± 1	

4.2.3 Optimization in Working Point 3 (49.16, 14.22)

From the reference configuration with corrected linear optics and orbit, the tunes were adjusted to the desired working point $(\nu_x, \nu_y) = (49.16, 14.22)$. IE in nominal conditions was low, indicating, as in WP2, deterioration of the DA when changing tunes.

The objective function was the average IE of 5 injection pulses in the same conditions as in WP1 and WP2 experiments. The optimization knobs were those of the Compensation Scheme described in section 3.3.2. Families SFP1 and SFB1 were not used and the search space was 13-dimensional.

Two optimization runs were carried out, starting from sextupole settings of the WP1 reference configuration. Best configuration found at run 1 was reloaded after magnets standardization and run 2 was launched. Only run 2 configuration was saved, and shall be referred to as the "optimized configuration". Figure 4.9 shows the objective

function history during the two optimization runs.
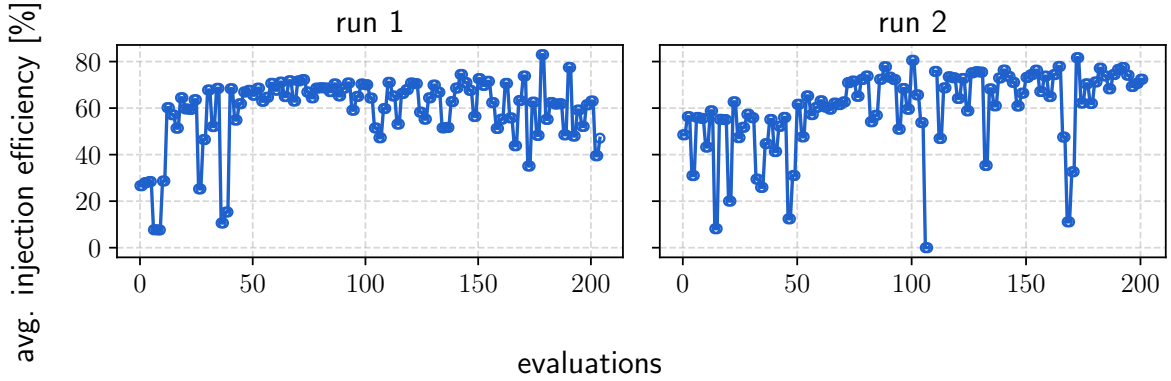
Figure 4.9: Objective function history during RCDS runs in WP3.

Characterization of the solution

The optimized solution was characterized in terms of kick resilience, phase space area, IE during nominal injection conditions and whether it preserved chromaticity and lifetime. Lifetime at 60 mA was measured at 19.5 hrs, so no significant reductions compared to the WP1 reference configuration were observed. No significant chromaticity changes were observed as well. Phase space area increased, compared to the initial non-optimized configuration, and reached similar value to that of the WP1 nominal tunes reference configuration, as Fig. 4.11 shows. Kick resilience, shown in Fig. 4.10, also improved, with a larger fraction of the beam surviving to large kicks in the range $700 - 770$ μrad. Finally, and most importantly, run 2 solution displayed IE of $93 \pm 3\%$ during nominal off-axis injection, which is acceptable for operating with this configuration.
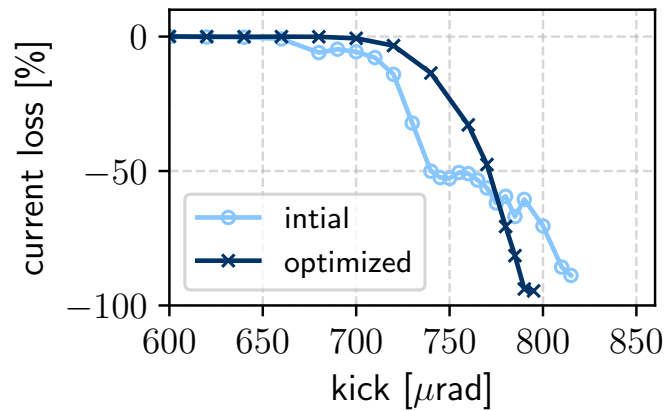
Figure 4.10: Current losses vs. horizontal dipole kick for the initial configuration and the RCDS solution at WP3.
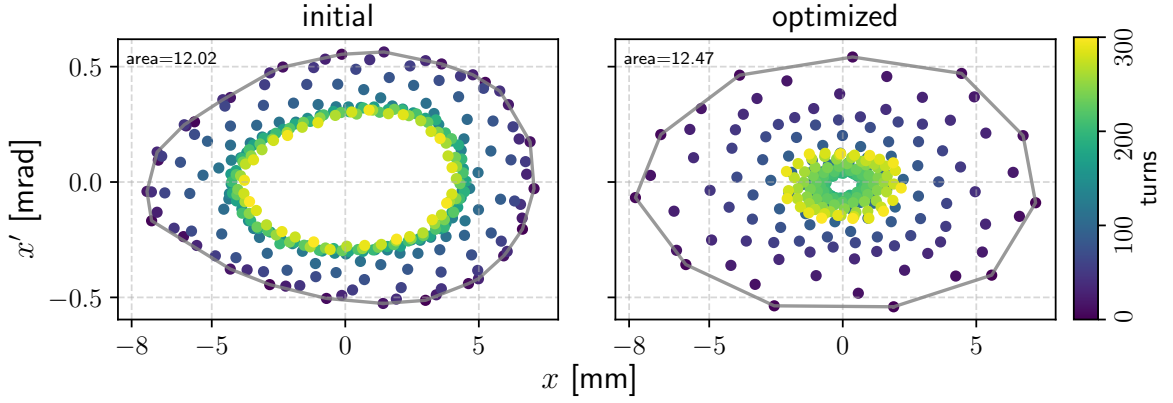
Figure 4.11: Measured phase space at SA05 high-beta straight section for the non-optimized configuration and the best RCDS configuration in WP3. Color-map indicates the turns. The areas are in mm mrad.

Summary of results

Table 4.3 summarizes the injection efficiencies achieved for the best configurations of each run and WP during nominal conditions for off-axis injection. Run 2 from WP1 and the optimzed configuration at WP3 were the best performing configurations of their corresponding WPs and successfully met the standards to be used during operation. Currently, WP3 is SIRIUS' working point and the optimized sextupole configuration identified in the online optimization experiments is deployed in the machine.

Table 4.3: Injection efficiencies (IE) for sextupole configurations found during online optimization at Working Points 1, 2 and 3.

WP1 (49.08, 14.14)		WP2 (49.20, 14.25)		WP3 (49.16, 14.22)	
configuration	IE [%]	configuration	IE [%]	configuration	IE [%]
ref. config.	88 ± 8	initial	51 ± 1	initial	
run 1	91 ± 1	run 1	79 ± 3	optimized	93 ± 3
run 2	98 ± 1	run 2	65 ± 1		
run 3	87 ± 3				

Orbit stability improvements

The motivation for exploring higher tunes was the desirable effect of reducing orbit amplification factors to improve the overall orbit stability. Orbit stability improvements in WP3 tunes were confirmed by the orbit integrated spectrum density of the orbit data collected with BPMs. The spectrum decreased by a factor of approximately 2, as Fig. 4.12, presented in Ref. [10], shows.

Leveraging WP3, and the improvements of the Fast Orbit Feedback System in 2023, orbit root-mean-square (rms) variations reached the record values of less than 1% of the horizontal beam size, in the horizontal plane, and less than 4% of the vertical beam size in the vertical plane [10]. New measurements indicate variations less than 2% the beam size for both the horizontal and vertical orbit.
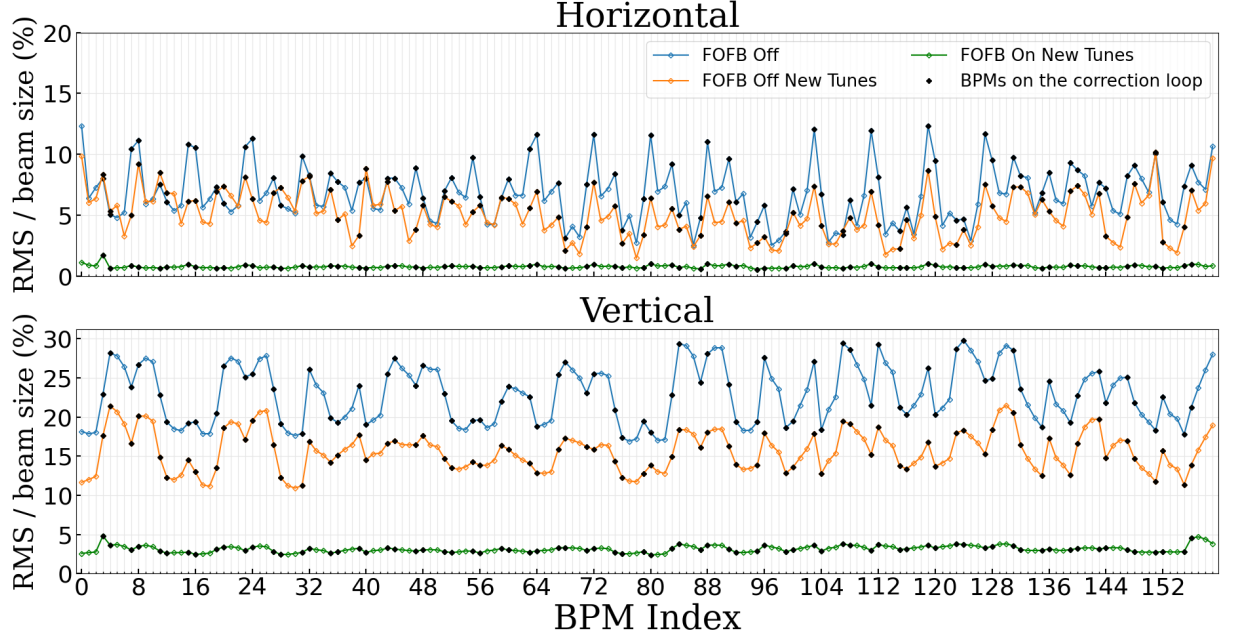
Figure 4.12: Horizontal (vertical) RMS orbit variations in units of the horizontal (vertical) beam sizes. Blue curves represents orbit variations in the nominal working point, WP1, orange curves are the orbit variations at WP3, and green curves variations at WP3 under the effects of the recent improvements in Fast Orbit Feedback System. From Ref. [10]

4.3   Amplitude-dependent tune-shift analysis

Online optimization is a heuristic optimization approach. It consists on exploring parameter space searching for regions where the DA and IE improve. One may wonder if any of the RCDS-optimized sextupole configurations share any common characteristic or trend that could explain why they improve the dynamics overall.

An intrinsic feature of nonlinear dynamics and relatively easy to access experimentally are the nonlinear tune-shifts. Specifically, the transverse amplitudes tune-shifts. By kicking the beam with the dipolar kicker at high strengths and acquiring TbT BPM data one can sample the large-amplitude betatron motion and fit it in the time domain to extract the fundamental frequency, which is the tune. Repeating this analysis for several kicks, ranging from 500 μrad up to 850 μrad, the amplitude-dependent tune-shift $\Delta\nu$ can be measured. Doing so gives the curve of tune-shifts vs dipolar kicks strengths. Using TbT data and eq. (9) of Ref. [38], the betatron action J can be fitted instead, and the curve of tune-shifts vs amplitudes J can be obtained. For the determination of tunes, the time-domain fitting of BPM data is carried out for each one of the 160 BPMs. The average tune is adopted as the estimate for the beam's tune, and the standard deviation as the error bar.

This analysis was performed for each RCDS sextupole configuration in the 3 working points, specializing to the horizontal tune-shifts due to horizontal kicks. That is, the beam was kicked in the horizontal direction, and the tunes of the induced horizontal betatron motion were calculated. The $\Delta\nu_x$ vs. J_x curves are shown by Fig. 4.13 for each
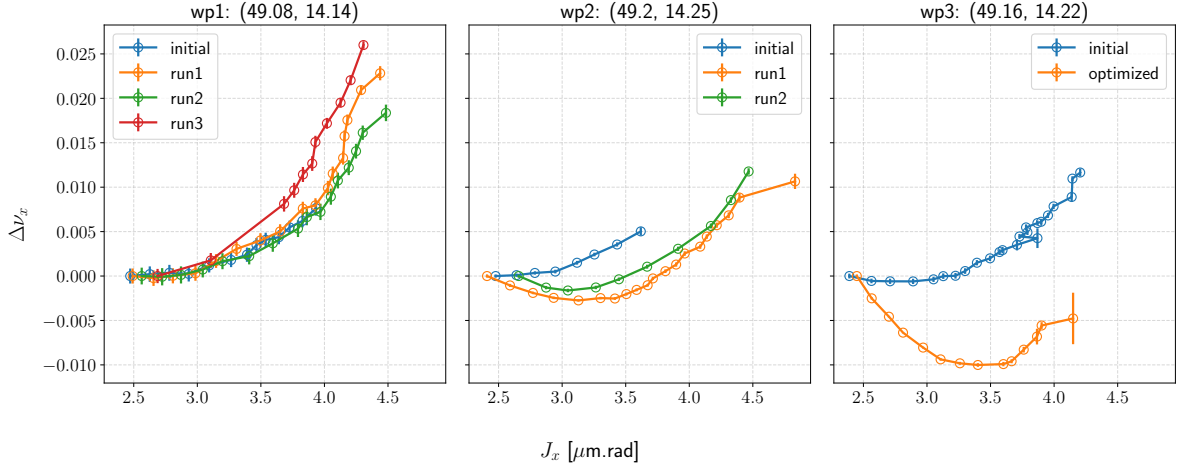
Figure 4.13: Horizontal tune-shifts vs. horizontal betatron actions for the RCDS solutions in WPs 1, 2, and 3.

configuration of the RCDS runs in each working point.

The common feature among the curves of the best performing configurations for each WP (run 2 for WP1, run 1 for WP2 and the optimized curve for WP3) in Fig. 4.13 seems to be the consistent departure from the nominal model curve (in blue), towards negative tune-shifts values. This trend for tune-shifts seems to be beneficial for the machine.

The same procedure can be done kicking the beam in the vertical direction and calculating the vertical motion tunes, giving the curve of $\Delta\nu_y$ vs. J_y. However, this experiment has not yet been carried out.

With the horizontal kicks data, attempts were also made to extract vertical tune shifts $\Delta\nu_y$ vs horizontal action J_x. However, due to coupling, it is difficult (and in most cases impossible) to extract the vertical tune from the y TbT BPM data, because the time-series gets contaminated with the horizontal tune signal and the vertical tune signal has a low signal-to-noise ratio.

One way to overcome these limitations is to change the experimental acquisition slightly: first, the beam must be kicked in the vertical direction once to induce a significant betatron motion and, consequently, increase the ν_y peak in the spectrum. This addresses the low signal-to-noise ratio limitation. After the vertical kick, the beam is then kicked in the horizontal direction with the kicks in the desired nonlinear dynamics range. This last step takes the beam to the large horizontal amplitudes optics, changing the vertical tune of the vertical motion induced in the first step according to what is prescribed by the nonlinear effects.

Characterizing the $\Delta\nu_x$ vs. J_x and the $\Delta\nu_y$ vs. J_x or $\Delta\nu_x$ vs J_y curves, one can reconstruct the path traced in the tune-space at large amplitudes. If the observed path avoids particular regions of the tune-space or particular resonance lines, the enhanced performance would be justified: the best-performing sextupole configurations are those

rendering beneficial behaviour in tune-space. Consequently, the dynamics is less irregular, less chaotic, specially close to the border of the DA, explaining the observed improvements in the IE, beam kick-resilience and phase space area.

Unfortunately, these additional data acquisitions and processing attempts could not be carried out before the completion of this dissertation. These tasks stands out as required next-steps if one wishes to understand and explain why these configurations rendered the improvements they did and also to verify the hypothesis that the optimized configurations render the dynamics with beneficial behaviour in tune-space.

CHAPTER 5

Conclusions

In this work, the Robust Conjugate Direction Search algorithm (RCDS) was studied, implemented in Python and applied to the problem of optimizing the nonlinear dynamics and dynamic aperture (DA) of the SIRIUS storage ring.

The experiments focused on using the average injection efficiency (IE) of five injection pulses as the objective function to probe the DA. While attempts were made using the beam's resilience to dipolar perturbations as the objective function, they did not yield satisfactory results in enhancing the IE in the nominal operation conditions. The average IE as objective function, on the other hand, proved to be a reliable figure of merit to access the DA.

The optimization parameters, or knobs, were the sextupole families of the storage ring. The need to optimize dynamics while maintaining constant chromaticity imposed constraints to the selection of families or combinations of families to be used as optimization knobs. Two methods were considered to ensure constant chromaticity: selecting combinations of sextupole families which belong to the null space of the chromaticity jacobian matrix; and selecting a reduced number of free optimization knobs and delegating an online scheme of chromaticity anticipation and correction to another set of sextupole families. We also experimented with imposing supplementary symmetries on the nonlinear lattice in the form of additional constraints to reduce the dimensionality of the search space. Optimization proved effective irrespective of the strategy employed to preserve chromaticity and the varying dimensions of the search space.

Optimization was conducted at the machine's nominal working point, denoted as Working Point 1 (WP1), with tunes $(\nu_x, \nu_y) = (49.08, 14.14)$ and two additional working points, WP2, with tunes $(\nu_x, \nu_y) = (49.20, 14.25)$, and WP3, with tunes $(\nu_x, \nu_y) = (49.16, 14.22)$. The optimization in WP1 was extremely successful, yielding a sextupole configuration that achieved the remarkable level of 98% IE in the nominal operational injection conditions. This configuration exhibited no adverse effects on chromaticity and beam lifetime while displaying an increased phase space area and enhanced kick resilience. In WP2, however, the optimization proved more challenging. Despite positive impacts on phase space areas, kick resilience, the resulting efficiency of 79% fell short of operational expectations. In contrast, the optimization in WP3 was deemed successful. The process

not only improved phase space areas and kick resilience but also achieved an IE of 93%, with no impact on lifetime and chromaticity.

The primary motivation for exploring different machine operation tunes was to elevate the fractional parts of the tunes, distancing them from integer resonances. This adjustment aimed to reduce orbit amplification factors, which quantify the sensitivity of the orbit to perturbations. The tunes of $(\nu_x, \nu_y) = (49.16, 14.22)$ of WP3, resulted in improved stability and IE in this WP was made possible due to the online optimization work. Leveraging this new working point and recent enhancements in the orbit feedback systems, the machine achieved a world-record orbit stability, with orbit variations of less than 2% of the beam size in both the vertical and horizontal orbits.

In conclusion, this study highlights the success of online optimization of nonlinear dynamics using RCDS in 4th-generation storage rings, exemplified by SIRIUS with its large parameter space. The outcomes of this work serve as a benchmark for the effectiveness of the RCDS method and advocate for the inclusion and planning of online optimization routines as a standard tools during the commissioning of future 4th-generation projects.

Bibliography

[1] Wiedemann, H. *Particle Accelerator Physics*. Graduate Texts in Physics (Springer International Publishing, 2015). URL http://link.springer.com/10.1007/978-3-319-18317-6.

[2] Huang, Z. Brightness and Coherence of Synchrotron Radiation and FELs. In *Proc. of the 4th Int. Particle Accelerator Conf. (IPAC 2013)* (JACoW, Geneva, Switzerland, May 12-17, 2013). URL https://accelconf.web.cern.ch/IPAC2013/papers/moycb101.pdf?n=IPAC2013/papers/moycb101.pdf.

[3] Hettel, R. O. Challenges in the Design of Diffraction-limited Storage Rings. In *Proc. of the 5th Int. Particle Accelerator Conf. (IPAC 2014)*, 7–11 (JACoW, Geneva, Switzerland, 2014). URL https://jacow.org/IPAC2014/papers/MOXBA01.pdf.

[4] Simoulin, V. The synchrotron generations. *Revue francaise de sociologie* **57**, 503–528 (2016). URL https://www.cairn-int.info/article-E_RFS_573_0503--the-synchrotron-generations.htm.

[5] Liu, L. & Westfahl, H. Towards Diffraction Limited Storage Ring Based Light Sources. In *Proc. of the 8th Int. Particle Accelerator Conf. (IPAC 2017)*, 1203–1208 (JACoW, Geneva, Switzerland, 2017). URL http://jacow.org/ipac2017/papers/tuxa1.pdf.

[6] Clarke, J. *The Science and Technology of Undulators and Wigglers*. Oxford Series on Synchrotron Radiation (Oxford University Press, 2004).

[7] Liu, L., Neuenschwander, R. T. & Rodrigues, A. R. D. Synchrotron radiation sources in Brazil. *Philosophical Transactions of the Royal Society A* (2019). URL https://royalsocietypublishing.org/doi/10.1098/rsta.2018.0235. Publisher: The Royal Society Publishing.

[8] SIRIUS beamlines. Official Website (2024). URL https://lnls.cnpem.br/beamlines/. Accessed 2024-02-09.

[9] Liu, L. *et al.* Status of SIRIUS Operation. In *Proc. of the 13th Int. Particle Accelerator Conf. (IPAC 2022)*, 1385–1388 (JACoW Publishing, Geneva, Switzerland, 2022). URL https://jacow.org/IPAC2022/papers/TUPOMS002.pdf.

[10] Liu, L. *et al.* Status of SIRIUS operation with users. In *Proc. of the 14th Int. Particle Accelerator Conf. (IPAC 2023)*, 2586–2589 (JACoW Publishing, Geneva, Switzerland, 2023). URL https://accelconf.web.cern.ch/ipac2023/pdf/WEOGA2.pdf.

[11] Sands, M. The Physics of Electron Storage Rings: An Introduction. Tech. Rep. SLAC-R-121, Stanford Linear Accelerator Laboratory (1969).

[12] Liu, L., Resende, X. R., Rodrigues, A. R. D. & de Sá, F. H. Injection Dynamics for SIRIUS Using a Nonlinear Kicker. In *Proc. of the 7th Int. Particle Accelerator Conf. (IPAC 2016)*, 3406–3408 (JACoW Publishing, Geneva, Switzerland, 2016). URL https://jacow.org/ipac2016/papers/THPMR011.pdf.

[13] de Sá, F. H., Liu, L. & Resende, X. R. Optimization of Nonlinear Dynamics for SIRIUS. In *Proc. of the 7th Int. Particle Accelerator Conf. (IPAC 2016)*, International Particle Accelerator Conference, 3409–3412 (JACoW Publishing, Geneva, Switzerland, 2016). URL https://jacow.org/ipac2016/papers/THPMR012.pdf.

[14] Dester, P. S., Sá, F. H. d. & Liu, L. Energy acceptance and on momentum aperture optimization for the SIRIUS project. *Journal of Physics: Conference Series* **874**, 012068 (2017). URL https://doi.org/10.1088/1742-6596/874/1/012068. Publisher: IOP Publishing.

[15] Huang, X., Corbett, J., Safranek, J. & Wu, J. An algorithm for online optimization of accelerators. *Nuclear Instruments and Methods in Physics Research Section A: Accelerators, Spectrometers, Detectors and Associated Equipment* **726**, 77–83 (2013). URL https://www.sciencedirect.com/science/article/pii/S0168900213006347.

[16] Huang, X. & Safranek, J. Online optimization of storage ring nonlinear beam dynamics. *Physical Review Special Topics - Accelerators and Beams* **18**, 084001 (2015). URL https://journals.aps.org/prab/abstract/10.1103/PhysRevSTAB.18.084001. ArXiv: 1502.07799.

[17] Liuzzo, S. M. *et al.* Rcds optimizations for the esrf storage ring. In *Proc. of the 7th Int. Particle Accelerator Conf. (IPAC 2016)*, 3420–3423 (JACoW Publishing, Geneva, Switzerland, 2016). URL https://jacow.org/ipac2016/papers/THPMR015.pdf.

[18] Olsson, D. K. Online Optimisation of the MAX IV 3 GeV Ring Dynamic Aperture. In *Proc. of the 9th Int. Particle Accelerator Conf. (IPAC 2018)*, 2281–2283 (JACoW Publishing, Geneva, Switzerland, 2018). URL http://accelconf.web.cern.ch/ipac2018/papers/WEPAL047.pdf.

[19] Yang, X. *et al.* Online Optimization of NSLS-II Dynamic Aperture and Injection Transient. In *Proc. of the 13th Int. Particle Accelerator Conf. (IPAC 2022)*, 1159–1162 (JACoW Publishing, Geneva, Switzerland, 2022). URL https://jacow.org/IPAC2022/papers/TUPOPT064.pdf.

[20] Velloso, M. M. S. *et al.* Online optimization of SIRIUS nonlinear optics. In *Proc. 14th International Particle Accelerator Conf. (IPAC 2023)*, 3302–3305 (JACoW Publishing, Geneva, Switzerland, 2023). URL https://accelconf.web.cern.ch/ipac2023/pdf/WEPL087.pdf.

[21] Lee, S.-Y. *Accelerator Physics* (World Scientific, 2004).

[22] Wolski, A. *Beam Dynamics In High Energy Particle Accelerators* (World Scientific, 2014).

[23] Huang, X. *Beam-based Correction and Optimization for Accelerators* (CRC Press, 2019).

[24] Landau, L. D. & Lifshitz, E. M. *The Classical Theory of Fields: Volume 2* (Butterworth-Heinemann, 1975).

[25] SÁ, F. H. d. *Study of impedances and collective instabilities applied to SIRIUS.* Ph.D. thesis, Instituto de Física Gleb Wataghin, Universidade Estadual de Campinas (2018). URL https://hdl.handle.net/20.500.12733/1633837.

[26] de Aguiar, M. A. M. *Tópicos de Mecânica Clássica* (2023). URL https://sites.ifi.unicamp.br/aguiar/files/2014/10/top-mec-clas.pdf. Accessed in 2024-02-26.

[27] Bartosik, H., Papaphilippou, Y. & Wolski, A. A first taste of nonlinear beam dynamics. *arXiv preprint arXiv:2201.01532* (2022). URL https://arxiv.org/abs/2201.01532.

[28] Arnold, V. I. Instability of dynamical systems with several degrees of freedom. *Doklady Akademii Nauk SSSR* **156**, 9–12 (1964).

[29] Press, W. H., Teukolsky, S. A., Vetterling, W. T. & Flannery, B. P. *Numerical Recipes 3rd Edition: The Art of Scientific Computing* (Cambridge University Press, 2007).

[30] Safranek, J. Experimental determination of storage ring optics using orbit response measurements. *Nuclear Instruments and Methods in Physics Research Section A: Accelerators, Spectrometers, Detectors and Associated Equipment* **388**, 27–36 (1997). URL https://www.sciencedirect.com/science/article/pii/S0168900297003094.

[31] Alves, M. B. *Linear optics and coupling corrections applied to SIRIUS commissioning.* Master's thesis, Instituto de Física Gleb Wataghin, Universidade Estadual de Campinas (201). URL https://www.repositorio.unicamp.br/acervo/detalhe/1162264?guid=1704720770863&returnUrl=%2fresultado%2flistar%3fguid%3d1704720770863%26quantidadePaginas%3d1%26codigoRegistro%3d1162264%231162264&i=4.

[32] Alves, M. B. Optics Corrections with LOCO on SIRIUS Storage Ring. In *Proc. of the 12th Int. Particle Accelerator Conf. (IPAC 2021)*, 825–828 (JACoW Publishing, Geneva, Switzerland, 2021). URL https://jacow.org/ipac2021/papers/MOPAB260.pdf.

[33] Olsson, D. K., Andersson, A. k. & Sjöström, M. Nonlinear optics from off-energy closed orbits. *Physical Review Accelerators and Beams* **23**, 102803 (2020). URL https://link.aps.org/doi/10.1103/PhysRevAccelBeams.23.102803. Publisher: American Physical Society.

[34] Li, Y., Xu, D., Smaluk, V. & Rainer, R. Nonlinear optics from hybrid dispersive orbits. *Nuclear Instruments and Methods in Physics Research Section A: Accelerators, Spectrometers, Detectors and Associated Equipment* **1060**, 169032 (2024). URL https://www.sciencedirect.com/science/article/pii/S016890022301032X.

[35] Powell, M. J. D. An efficient method for finding the minimum of a function of several variables without calculating derivatives. *The Computer Journal* **7**, 155–162 (1964). URL https://doi.org/10.1093/comjnl/7.2.155.

[36] Alves, M. B. *et al.* lnls-fac/apsuite: v2.50.0 (2023). URL https://zenodo.org/records/10391151.

[37] Liu, L., Resende, X. R. & de Sá, F. H. A New Optics for SIRIUS. In *Proc. of the 7th Int. Particle Accelerator Conf. (IPAC 2016)*, 3413–3416 (JACoW Publishing, Geneva, Switzerland, 2016). URL https://jacow.org/ipac2016/papers/THPMR013.pdf.

[38] Resende, X., Alves, M., Liu, L. & Sá, F. H. d. Equilibrium and Nonlinear Beam Dynamics Parameters From SIRIUS Turn-by-Turn BPM Data. In *Proc. of the 12th Int. Particle Accelerator Conf. (IPAC 2021)*, 1935–1938 (JACoW Publishing, Geneva, Switzerland, 2021). URL https://jacow.org/ipac2021/papers/TUPAB219.pdf.

APPENDIX A

Algorithms pseudocode

This appendix presents pseudocode for simplified versions of the routines implemented Python during the execution of this work. The code has been simplified for pedagogic reasons, focusing on the main characteristics of each routine composing the RCDS algorithm. In particular, the checking of data consistency and adequacy are not included; the bracketing and line scan routines are presented only for the simpler case of a single parameter optimization and the normalization of parameters range is not included. The RCDS Python code used in this work is available in "optimization/rcds.py", in the apsuite repository [36].

A.1   RCDS Bracketing

Given the initial point x_0, the initial value for the objective function $f_0 = f(x_0)$, and the initial step size, the bracketing routine scans "downhill" until the function stops decreasing and starts to increase by more than the 3σ threshold. The step size is increased at each evaluation by the golden ratio $\phi = \frac{1+\sqrt{5}}{2}$, as long as it does not exceed 0.10. The use of the golden ratio is inspired by the Golden Section Search bracket routine [29, sec. 10.2]. The bracketing function returns a list of x positions, which are the brackets, and the objective function evaluated at those points. Pseudocode is shown in Algorithm 1. The bracketing function calls the externally defined function "ObjectiveFunction()", which implements the evaluation of the figure of merit. This function increases the global variable "n_evals" whenever it is called. This keeps track of the number of objective function evaluations, which is essential as a stopping condition for Powell's loop.

A.2   RCDS line scan

In algorithm 2, the RCDS line scan function is presented. The list of positions within the brackets and measured objective functions must be provided alongside m, the number of points that should be sampled within the brackets, and n, the smallest number of points inside the brackets required for trusting the fit. Notice these are different parameters. If the provided list of positions is already of size m, no additional points are

---

Algorithm 1 RCDS bracketing

1: **function** BRACKETINGMIN(x_0, f_0, step)
2:     positions ← list containing x_0
3:     functions ← list containing f_0
4:     $x_{\min}$, $f_{\min}$ ← x_0, f_0
5:     dir ← $+x$ ▷ *scan in the positive direction*
6:     f ← ObjectiveFunction(x_0 + step)
7:     **if** $f < f_{\min}$ **then**
8:         $f_{\min}$ ← f
9:     append x_0 + step to positions
10:     append f to functions
11:     **while** $f < f_{\min} + 3\sigma$ **do**:
12:         **if** $|\text{step}| < 0.1$ **then**
13:             step ← step $\times (1 + \phi)$
14:         **else if** dir $= +x$ **then**
15:             step ← step + 0.1
16:         **else**
17:             step ← step - 0.1
18:         f ← ObjectiveFunction(x_0 + step)
19:         **if** f is NaN **then**
20:             **break**
21:         **if** $f < f_{\min}$ **then**
22:             $x_{\min}$ ← x_0 + step
23:             $f_{\min}$ ← f
24:         append x_0 + step to positions
25:         append f to functions
26:     **if** $f_0 \leq f_{\min} + 3\sigma$ **then**   ▷ *if false, no need to scan in the other direction*
27:         dir ← $-x$
28:         step ← $-$step
29:         start again from line 6   ▷ *scan in the negative direction*
30:     sort positions in ascending order
31:     sort the corresponding entries of functions in the same ordering as positions
32:     **return** positions, functions, $x_{\min}$, $f_{\min}$

---

sampled, otherwise, additional measurements are carried out. Once m points are available, the parabola is fitted and the outlier removal routine evaluates the measured points against the model. If any outliers are removed and the remaining number of available points is smaller than n, this means we cannot trust the model because too little points remained, according to the user-defined value.

Algorithm 2 RCDS line scan

1: **function** LINESCAN(positions, functions, $x_{\min}$, $f_{\min}$, n, m)
2:     $a \leftarrow$ positions first entry
3:     $c \leftarrow$ positions last entry   ▷ *brackets (a, x_{min}, c)*
4:     $V \leftarrow$ evenly spaced m-array w/ values $\in [a, c]$ ▷ *dense span inside the brackets*
5:     $f(V) \leftarrow m$-array with NaNs
6:     **for** the i-th entry of positions **do**   ▷ *reuse previously measured point*
7:         $j^* \leftarrow \operatorname{argmin}_j(|V[j] - \text{position}[i]|)$
8:         $V[j^*] \leftarrow \text{position}[i]$
9:         $f(V)[j^*] \leftarrow \text{functions}[i]$
10:     **for** the i-th entry of V which is NaN **do**
11:         ▷ *measure the points not measured yet*   ◁
12:         $f(V)[i] \leftarrow \text{ObjectiveFunction}(V[i])$
13:     c_0, c_1, $c_2 \leftarrow \text{CalcDeg2PolynomCoefs}(V, f(V))$
14:     V, $f(V) \leftarrow \text{RemoveOutiler}(V, f(V))$
15:     **if** length$(V) < n$ **or** $c_2 \leq 0$ **then**
16:         ▷ *no sufficient points for trusting the fit or wrong parabola concavity*   ◁
17:         **return** $x_{\min}$, $f_{\min}$
18:     $V \leftarrow$ evenly spaced 1000-array w/ values $\in (a, c)$
19:     $f(V) \leftarrow$ empty 1000-array
20:     **for** the i-th entry of V **do**
21:         ▷ *fine scan for min on the parabolic model*   ◁
22:         $f(V)[i] \leftarrow c_0 + c_1 V[i] + c_2 V[i]^2$ ▷ *$f(V) = [f(a), \ldots, f(c)]$*
23:     $x_{\min} \leftarrow V[\operatorname{argmin}(f(V))]$
24:     $f_{\min} \leftarrow \min(f(V))$
25:     **return** $x_{\min}$, $f_{\min}$

The function references the externally defined functions "ObjectiveFunction()" "RemoveOutlier()" and "CalcDeg2PolynomCoefs()". Pseudocode for the RemoveOutlier() function is not essential here, since its implementation is simple and offers small pedagogic value for our purpose. The reader may check our python implementation of the "remove outlier" function in the "RCDSParams" class of the "rcds.py" file of the "apsuite" repository. The conceptual idea of the routine is:

1. calculate the errors as the differences between observed and fitted values.

2. sort the errors and compute the differences between consecutive errors.

3. if there are less than 5 points evaluated within the brackets, check if the largest and smallest differences are greater than a threshold 3σ. If yes, exclude the corresponding

points.

4. calculate the average of the errors differences (errors standard deviation) within a
   specified percentile range. Identify outliers based on differences exceeding a threshold
   3σ for both larger and smaller differences. Create a boolean mask to mark outliers
   and return the filtered array of x positions and objective function measurements.

The "CalcDeg2PolynomCoefs()" function implements the parabolic fit within
the brackets and returns the zeroth, first and second degree coefficients c_0, c_1, c_2 for which
the polynomial $c_0 + c_1 x + c_2 x^2$ best explains, in the least-squares sense, the observed data.

A.3   Powell's method

Algorithm 3 presents the pseudocode for the main loop in the optimization
routine. It implements Powell's method for constructing new directions with ref's. [29,
section 10.7] criteria for when to replace directions and stop the routine. Stopping
conditions can be reached by the maximum number of objective function evaluations
the user specifies, or according to a tolerance value for deciding when the objective has
changed significantly.

Again we stress that the bracketing and line scan pseudocode presented above,
as well as Powell loop below, were significantly simplified for pedagogic reasons. In
particular, 1-dimensional versions for the bracketing and line scan were presented, omitting
the the extra steps of reducing the high-dimensional minimization problem into a 1-
dimensional problem of minimizing $g(\delta) = f(\mathbf{x}_0 + \delta\mathbf{u}_i)$ for a direction $\mathbf{u}_i$. Additionally, in
Powell's loop, the RCDS code normalizes the knobs in the $[0, 1]$ interval, so the parameter
space consists on a unit hypercube. Handling of normalization and de-normalization to
evaluate the objective function is also omitted here.

Algorithm 3 Powell directions loop

1: **function** OPTIMIZE(max_evals, search_dirs, step, tol, $\mathbf{x}_0$, ortho_threshold)
2:      max_decrease $\leftarrow 0$
3:      max_decrease_dir $\leftarrow 0$
4:      $f_0 \leftarrow$ ObjectiveFunction($\mathbf{x}_0$)
5:      $\mathbf{x}_{\min} \leftarrow \mathbf{x}_0$
6:      $f_{\min} \leftarrow f_0$
7:      **for** i-th direction vector $\mathbf{u}_i$ in search_dirs **do**
8:          positions, functions, $\mathbf{x}_{\min}$, $f_{\min} \leftarrow$ BracketingMin($\mathbf{x}_0$, f_0, step)
9:          $\mathbf{x}, f \leftarrow$ LineScan(positions, functions, $\mathbf{x}_{\min}$, $f_{\min}$)
10:         **if** $f_{\min} - f >$ max_decrease **then**
11:            max_decrease $\leftarrow f_{\min} - f$
12:            max_decrease_dir $\leftarrow i$
13:         $\mathbf{x}_{\min} \leftarrow \mathbf{x}$
14:         $f_{\min} \leftarrow f$
15:         $\mathbf{x}_e \leftarrow 2\mathbf{x}_{\min} - \mathbf{x}_0$ ▷ *define extension point*
16:         $f_e \leftarrow$ ObjectiveFunction($\mathbf{x}_e$)   ▷ *evaluate objective at extension point*
17:         $\mathbf{u}_{\text{new}} \leftarrow \frac{\mathbf{x}_{\min} - \mathbf{x}_0}{|\mathbf{x}_{\min} - \mathbf{x}_0|}$ ▷ *new proposed direction*
18:         max_dot $\leftarrow 0$ ▷ *max overlap w/ all the directions*
19:         **for** j-th direction vector $\mathbf{u}_j$ in search_dirs **do**
20:            dot $= \mathbf{u}_j \cdot \mathbf{u}_{\text{new}}$
21:            **if** dot $>$ max_dot **then:**
22:              max_dot $\leftarrow$ dot
23:         cond1 $\leftarrow f_0 \leq f_e$
24:         cond2lhs $\leftarrow 2(f_0 - 2f_{\min} + f_e)(f_0 - f_{\min} - \text{max\_decrease})^2$
25:         cond2rhs $\leftarrow$ max_decrease$(f_e = f_0)^2$
26:         cond2 $\leftarrow$ cond2lhs $\geq$ cond2rhs
27:         **if** cond1 **or** cond2 **then**
28:            ▷ *Numerical Recipes conditions for direction replacement*   ◁
29:            **output** max_decrease_dir not replaced
30:         **else if** max_dot $<$ orth_threshold **then**
31:            ▷ *If conditions are met and new dir sufficiently orthogonal, replace*   ◁
32:            **output** replacing max_decrease_dir
33:            $\mathbf{u}_i \leftarrow \mathbf{u}_{i+1}$ **for** $i = 1, \ldots, p-1$
34:            $\mathbf{u}_p \leftarrow \mathbf{u}_{\text{new}}$
35:            ▷ *and minimize along new direction*   ◁
36:            positions, functions, $\mathbf{x}_{\min}$, $f_{\min} \leftarrow$ BracketingMin($\mathbf{x}_0$, f_0, step)
37:            $\mathbf{x}_{\min}, f_{\min} \leftarrow$ LineScan(positions, functions, $\mathbf{x}_{\min}$, $f_{\min}$)
38:         **else**
39:            **output** max_decrease_dir not replaced
40:         cond $\leftarrow 2|f_0 - f_{\min}| \leq$ tol$(|f_0| + |f_{\min}|)$
41:         **if** cond **and** tol> 0 **then**
42:            **output** Stopping condition met. Exiting
43:            **break**
44:         **else if** n_evals $>$ max_evals **then**
45:            Maximum number of objective function evaluations reached. Exiting
46:            **break**
47:         $f_0 \leftarrow f_{\min}$
48:         $\mathbf{x}_0 \leftarrow \mathbf{x}_{\min}$